SIEMENS

White Paper | siemens.com/mi

Introduction to xSPECT* Technology: Evolving Multi-modal SPECT to Become Context-based and Quantitative

A. Hans Vija, PhD, Siemens Molecular Imaging

Table of Contents

Introduction: The Motivation to Evolve Multi-modal SPECT and the Concept of xSPECT **1**

Motivation to evolve SPECT/CT 1

The concept of xSPECT 1

The Technology Behind xSPECT **2**

Motivation to move on from ML-EM-based reconstruction 2

The fundamentals of the xSPECT reconstruction platform 2

Improving the accuracy of the image formation model 3

The First Application: xSPECT Bone **7**

The concept of context-sensitive reconstruction 7

Implementing extra-modal information into the reconstruction 7

Generation of the zone map for the ^{99m}TC Di-Phosphonate application 7

The Multi-modal reconstruction algorithm 7

Testing the concept: probing the obvious pitfalls with phantoms 9

Testing the concept: clinical feasibility 13

Evaluations of xSPECT Bone 15

Concordance evaluation 15

Clinical example 21

The Second Application: xSPECT Quant **22**

xSPECT's quantitative foundation: NIST traceable calibration and rigorous data handling 22

Evaluations of xSPECT Quant 23

Clinical example 24

Summary **24**

Acknowledgment **25**

Glossary **25**

References **26**

**Symbia Intevo™ and xSPECT are not commercially available in all countries. Due to regulatory reasons, their future availability cannot be guaranteed. Please contact your local Siemens organization for further details.*

Introduction: The Motivation to Evolve Multi-modal SPECT and the Concept of xSPECT

Motivation to evolve SPECT/CT

Molecular imaging systems depict and measure biochemical processes *in-situ* and require advancements in multi-modality systems, molecular biology, and probe development to help fulfill the desire of substantially increased diagnostic power.[1,2] In clinical practice, such systems help enable the physician to find, characterize, and follow disease over time. These requirements represent a technical challenge, and ultimately establish the need for both structural and functional data.

Such data should be acquired in an optimal fashion for the task at hand, and is typically done with dedicated imaging methods driven by various customizable parameters. Siemens introduced the Symbia™ series in 2005 by mechanically integrating a fully diagnostic-capable CT system with a SPECT system–at that time a unique concept. However, Symbia is ultimately still a SPECT system, with functional data acting as the primary source of information and the CT data as secondary. This arrangement of priorities manifested itself in CT images which were normally of lower quality than that actually allowed by the system. In other words, the view point was SPECT-centric.

In June 2013, Siemens introduced xSPECT technology, which represents a more complete integration of SPECT and CT data as compared to conventional SPECT/CT systems.

The concept of xSPECT

In order to depict and measure biochemical processes *in-situ* one needs to get information from inside the body to a detector outside the body. One method is SPECT imaging, where a tracer is injected into the patient. This tracer is radioactive, and emits photons that traverse the body (e.g., 140 keV photons for ^{99m}Tc), and are mostly absorbed by a cost-efficient detector. The SPECT image formation process is based on a collimator rejecting emitted photons which do not meet specific angular acceptance criteria. Roughly, only 1 out of every 10,000 photons emitted reach the detector and they carry directional information that can be used in a subsequent image reconstruction. Directional information is an example of Intra-Modal Information (IMI) that is used to improve reconstruction, for instance, by including a distant-dependent collimator Point Spread Response Function (PSRF) and collimator hole direction in the reconstruction. Clinical SPECT is radiation dose limited, and thus such a detector must be very sensitive. SPECT detectors can image the impact of a single tracer-emitted photon. The price for such sensitivity is poor resolution. A CT scanner, on the other hand, delivers and detects many orders of magnitude and more photons that allow for much finer spatial resolution. Typically, a doubling of resolution requires an eight-fold increase in dose at the same noise level[3,4] yet, regardless of the technical implementation, the more photons with directional information that are detected, the higher the resolution of the system. Fact is, SPECT and CT do operate at different ends of the resolution spectrum or respective sensitivity, because of the requested primary clinical imaging needs of each modality. The acquisition design is optimized for the two modalities and thus distinctly different, but once data are obtained one can ask what benefits can we gain when the information from the data is integrated?

We want to extract as much information as possible from the structural data, and use that Extra Modal Information (EMI) to assist the reconstruction of the functional data.

Thus, a basic idea is to take better advantage of the sharper spatial resolution of the CT and the anatomical information contained therein, and thus we also need to preserve its spatial accuracy. In essence, we adopt a more structure-centric view point. The "x" in xSPECT represents the data integration of the two modalities, and a reminder of the change of the frame-of-reference from SPECT to CT.

xSPECT reconstruction uses the CT coordinate system as its reference system of choice to minimize interpolation errors of the information obtained from the anatomical modality, and the resulting reconstructed xSPECT image is created in a CT equivalent slice-by-slice DICOM format.

The preservation of greater spatial accuracy is enabled by requiring a denser spatial sampling of the functional data. For instance, to improve alignment of data (registration) and subsequently to make better use of the information contained in the high resolution CT, we use smaller pixel sizes and larger matrices. It may seem counter intuitive to increase the matrix size, as this increases the number of estimable parameters cubically and thus decreases the count density (count per pixel), a process which typically degrades reconstructed image quality. However, this unwanted side effect can be mitigated if the image formation and reconstruction method is improved in tandem.

The underlying technology of xSPECT improves the image formation model, better preserves data characteristics, and opens a pathway to further integrate system- and application-specific context information into the emission tomography reconstruction process. These improvements more than make up for the increase in matrix size and its potential limitations.

The idea of integrating context into the reconstruction is motivated by the way physicians read medical images. Just as a physician uses his or her knowledge and experience, along with the patient's history and other diagnostic information provided by other tests when reading an image, we want to provide the reconstruction with additional information as well. By changing from a SPECT- to a CT-centric view and using advances in the underlying technologies, we can harness these benefits to assist the reconstruction of the xSPECT emission data. This amalgamation concept of multi-modal data has a range of potential applications, but we start with a clinical application, single photon bone imaging, that has three significant advantages:

1. The application has a high volume, and is well established,
2. There is minimal need for advanced registration solutions, where rigid body registration is mostly well justified, and
3. The Di-phosphonate uptake is correlated to bone turnover with a high signal-to-background ratio, and bone tissue is well imaged on a CT.

The field has a lot of experience with the bone application and its clinical workflow of planar/wholebody bone imaging, and SPECT as well as the familiar tracer, yet it is exactly this familiarity that allows for new concepts to be introduced and evolved. We anticipate the xSPECT concept may lead to further improvements in patient care.

xSPECT technology enables Symbia Intevo to become quantitative: Symbia Intevo with xSPECT technology can measure activity concentration in Bq/ml at locations within the FOV. We introduce a NIST traceable calibration where we use a specifically designed ^{57}Co source to calibrate Symbia Intevo to an absolute standard, minimizing detector performance variability.

Improvements in image quality, enabled by more accurate system modeling and a more powerful reconstruction engine also allow for more efficient use of available counts, maintaining excellent image quality for lower-count studies. In conjunction with dedicated solutions, such as IQ•SPECT, or Enhanced Planar Processing, we provide solutions for faster scanning or scanning at lower dose.

All these advancements, in particular the introduction of quantitative procedures, may be augmented by automation. The Automated Quality Control (AutoQC) package and Automated Collimator Changer (ACC), lower the burden on technologists and increase overall efficiency.

The Technology Behind xSPECT

Motivation to move on from Maximum Likelihood Expectation Maximization (ML-EM)-based reconstruction

The most widely used iterative reconstruction technique in clinical practice today is based on Ordered Subset Expectation Maximization (OSEM), derived in 1994 by Hudson and Larkin[5], which is itself based on MLEM.[6] The current Flash3D reconstruction engine belongs to this family of methods.[7] In the case of SPECT, tomographic image reconstruction takes the form of an ill- conditioned inverse problem[8, 9] using noisy data, where the number of estimable parameters is roughly the same as the number of data points. In contrast to Filtered Back Projection (FBP), iterative reconstructions exhibit non-stationary noise with a structure that changes across the FOV. In the case of MLEM (OSEM with 1 subset), the noise magnitude (variance) increases with increasing counts.[10] Nuyts confirmed that the image of the variance in unsmoothed MLEM images is very similar to the image of the mean values. The variance is therefore higher in regions of high activity, where diagnostic information resides.[11] Furthermore, noise correlation properties are iteration-dependent, and it has been shown that noise characteristics have ramifications on lesion detection tasks.[12, 13]

The Maximum Likelihood method was originally introduced by Fisher in 1912[14], who subsequently described its limitations in 1928.[15] Specifically, Fisher cited the case where the number of data points is roughly equal to the number of estimable parameters to be one for which the ML estimation process is poorly suited. In emission tomography, this is precisely the regime within which we must operate.

To guard against image noise resulting from this fundamental pitfall and achieve interpretable images, we terminate the reconstruction early and apply post smoothing. We accept that with this procedure we have resolution and noise characteristics that vary across the image due to the finite number of updates. Nevertheless, despite this drawback, this strategy is in clinical use because it produces visually pleasing results and allows for efficient compensation for the physics of the image formation process via procedures such as attenuation and scatter correction.

The ML-EM update mechanism is derived by maximizing the Poisson likelihood, yet the update formula itself is insensitive to the data statistics. For instance, simply scaling data by a constant factor has little effect on the ML-EM reconstruction, yet clearly the data is no longer Poisson.

A typical ML-EM implementation uses a multiplicative update mechanism, where the update factor is positive, semidefinite, and essentially a ratio comparing the data and data model, which appears in the denominator. In Flash3D, we limit the denominator to a minimum threshold, avoiding the division by zero or very small numbers and thus not allowing the ratio to become too large. The choice of this minimum threshold, in conjunction with the multiplicative update method, gives rise to an "evaporation" effect, wherein counts in regions of low activity gravitate towards regions of high activity. Lowering this threshold value will yield noisier images, and increasing the threshold will increase the evaporation effect.

Our goal is to design a quantitative reconstruction platform, which attempts to overcome some of the aforementioned shortcomings of an MLEM method. We want a faster resolution recovery per unit noise measure for extended objects, an improvement in cold lesion contrast and a highly adaptable reconstruction platform, that allows us to integrate all of our multi-channel collimators and application context-sensitive information.

The fundamentals of the xSPECT reconstruction platform

Each iterative reconstruction algorithm consists of an optimization method and an objective function upon which this optimizer operates. For xSPECT, we chose the χ^2 as a merit function, which for Gaussian noise is quadratic in the data model and therefore has a linear gradient. The problem with the traditional χ^2, however, is that the variance of Poisson counts is equal to its expectation

value, rendering it again nonlinear and ill-behaved in the low count regime. Modified versions of the χ^2 have therefore been proposed by Mighell.[16] We use Mighell's χ^2_γ merit function

$$\chi^2_\gamma = \sum_i \left[d_i + \mathrm{Min}\left(d_i, 1\right) - m_i \right]^2 \Big/ \left(d_i + 1\right), \qquad (1)$$

because it yields unbiased data models at low counts. In this notation d_i are the actual counts at pixel *i*, equal to the forward projected noiseless mean of the data $\tilde{m}_i$ Poisson noise n_i

$$d_i = \tilde{m}_i + n_i \quad \forall \mathrm{i} \ . \qquad (2)$$

As the noiseless mean $\tilde{m}_i$ is not accessible, we construct a model m_i to estimate the $\tilde{m}_i$ from the data using an image estimate I_α. The model of estimated detection events is equal to

$$m_i = \sum_\alpha H_{i\alpha} I_\alpha \quad \forall \mathrm{i} \qquad (3)$$

I_α represents the functional activity concentration, in units Bq/ml and $H_{i\alpha}$ represents one element of the system matrix *H*, corresponding to the probability that a photon originating at 3D voxel α is detected at the *i*-th 2D detector element. Here, α stands for all the variables that characterize the functional activity: 3D position, time, and photon energy. In practice, α is discretized into 3D voxels subdivided into time and energy bins. We refer to α generically as a "voxel" index, despite these additional time and energy components. The contribution of scattered photons s_i to the data model is estimated separately and must be added to the algorithm. Eq. (3) thus becomes

$$m_i = \sum_\alpha H_{i\alpha} I_\alpha + s_i \quad \forall \mathrm{i} \qquad (4)$$

The system matrix H is rarely applied directly as a matrix multiplication and is implemented instead via the serial application of operators H_k, as follows:

$$H = H_k \otimes \ldots \otimes H_2 \otimes H_1 \qquad (5)$$

The adjoint of the forward projection, representing the backward projection from the data space into object space, may be described as an application of the transpose H^T of the system matrix, alternatively expressed in the following equation:

$$I_\alpha = \sum_i H_{\alpha i} m_i \ . \qquad (6)$$

The transpose H^T is also rarely applied as a matrix multiplication. Instead, it is similarly represented as a product of operators:

$$H^T = H_1^T \otimes H_2^T \otimes \ldots \otimes H_k^T \qquad (7)$$

xSPECT uses the conjugate gradient minimization scheme to minimize the χ^2_γ merit function. For more details on his method, see, e.g., Press et al, 2007.[17] The use of the conjugate gradient in SPECT reconstruction was discussed by Tsui, et al in 1991.[18]

** Convergence implies that the absolute minimum (xSPECT), or maximum (MLEM) of the objective function in question is reached. In practice, convergence in this sense is intentionally avoided, as it would require an excessive number of iterations and would produce noisy, diagnostically useless images. Instead, a point of convergence is sought beyond which the diagnostic content of the image will cease to increase, but before the onset of degrading noise accumulation.*

Improving the accuracy of the image formation model

In order to achieve quantitative accuracy and improve image quality, the system must be characterized accurately. A further challenge is the incorporation of this information within the reconstruction in a computationally efficient manner to prevent excessive processing times. That subject is not included in the scope of this paper.

As mentioned above, we use the conjugate gradient method, which is known to converge* quadratically[18] and requires fewer updates than MLEM to achieve the same resolution recovery, albeit at the cost of a correspondingly more rapid pace of noise accumulation.

The goal is to achieve noise build-up that is slower than the resolution recovery, otherwise there is no gain for a slower converging method.

In order to mitigate the noise build-up, a number of steps were taken. The most fundamental is the aforementioned Mighell χ^2_γ merit function, which assumes Poisson data. It is sensitive to noise statistics. With the sensitivity of this objective function in mind, it is important that the acquired data remain unaltered during reconstruction. For this reason, all operations during xSPECT reconstruction are performed in the image space.

Inaccuracies in the system model propagate with each forward- and back-projection throughout the entire reconstruction process and are potentially a major source of systematic errors. Thus, a second component is to mitigate systematic noise by using a more accurate system model.

The image formation model of xSPECT employs the following improvements:

i. Adaptive 3D Gantry Deflection Matrix: 3D rotation and translation to incorporate the optically measured Gantry Deflection matrix for the Symbia family (class standard). This matrix is adapted to each specific system for further accuracy;
ii. Collimator Angulation Measurement: vector map characterizing the direction in which each collimator hole points, which is either measured for each collimator (**SMART**ZOOM) or based on a class standard (LEHR);
iii. Accurate Point Spread Response Function (PSRF): 3D distance-dependent Point Spread Response Function that is either measured for ^{99m}Tc over the entire FOV and includes the septal penetration response, or derived from the hole geometry in the case of **SMART**ZOOM (i.e., no longer Gaussian);
iv. View-dependent decay correction;
v. Attenuation correction during both forward- and back-projection;
vi. Energy window-based scatter correction, where a smoothed scatter projection estimate is added to the data model.

The previously used conversion from CT Hounsfeld units to a linear attenuation coefficient map is unchanged, and is based on our patented transformation method of adaptive bi-linear conversion.[19,20] Estimation of the scatter in the primary window is based on the work by Ichihara.[21]

A comparative summary of the key features of iterative reconstruction solutions used on Symbia Intevo is depicted in Figure 1:

Siemens Symbia Intevo Reconstruction Solution Comparison

Reconstruction Method	Flash3D	xSPECT	xSPECT Bone	xSPECT Quant	IQ•SPECT
Dicom Output Type	NM RECON TOMO	NM RECON TOMO	NM RECON TOMO or PET	PET	NM RECON TOMO
Output unit (Dicom Unit)	counts (cnts)	Bq/ml (propcps)	Bq/ml (propcps or Bqml)	Bq/ml(Bqml)	Bq/ml (cnts)
Post Smoothing	3D Gaussian	3D Gaussian	zonal boundary preserving 3D Gaussian for each zone	3D Gaussian	3D Gaussian
Extra Modal Information (EMI) Method	N/A	N/A	linear combination with zonal Forward Projection	N/A	N/A
EMI Generation			CT derived zones for 99mTc Di-Phosonate application.		
Scatter Compensation	Optional: Additive in Forward	Additive in Forward Projector	Additive in Forward Projector	Additive in Forward Projector	Additive in Forward Projector
Scatter Projection Estimate (SPE)	Smoothing of SPE. Default: 0 Energy Window based per peak (DEW or TEW).	Smoothing of SPE. Default: Energy Window based per peak (DEW or TEW).	Smoothing of SPE. Default: Energy Window based per peak (DEW or TEW).	Smoothing of SPE. Default: Energy Window based per peak (DEW or TEW).	Smoothing of SPE. Default: 0 Energy Window based per peak (DEW or TEW).
Attenuation Compensation Method	Optional: Voxel based in Forward/Backprojector	Optional: Voxel based in Forward/Backprojector	Voxel based in Forward/Backprojector	Voxel based in Forward/Backprojector	Optional: Voxel based in Forward/Backprojector
Linear Attenuation Coeffcient (LAC) or "mu-map" Generation	Smoothing. Default: 0 mm CT derived. Adaptive (patient, scan, energy window), bi linear conversion based on fit to reference materials.	Smoothing. Default: 0 mm CT derived. Adaptive (patient, scan, energy window), bi linear conversion based on fit to reference materials.	Smoothing. Default: 0 mm CT derived. Adaptive (patient, scan, energy window), bi linear conversion based on fit to reference materials.	Smoothing. Default: 0 mm CT derived. Adaptive (patient, scan, energy window), bi linear conversion based on fit to reference materials.	Smoothing. Default: 0 mm CT derived. Adaptive (patient, scan, energy window), bi linear conversion based on fit to reference materials.
Resolution Recovery Method	Forward/Backprojector	Forward/Backprojector	Forward/Backprojector	Forward/Backprojector	Forward/Backprojector
PSRF Model	Depth Dependent based on measured ROR 3D Gaussian.FWHM adjusted for Septal Penetration	Depth Dependent based on measured ROR Acquisition window specific measured PSRF map over entire FOV	Depth Dependent based on measured ROR Acquisition window specific measured PSRF map over entire FOV	Depth Dependent based on measured ROR Acquisition window specific measured PSRF map over entire FOV	Depth Dependent based on measured ROR 3D geometric hole model convolved with intrisinsic resolution
Collimator Vector Map	N/A	LEHR Class standard	LEHR Class standard	LEHR Class standard	Measured 3D individual SMARTZOOM "Vectormap fingerprint"
Supported collimators	UHR,LEHR, LEAP,MELP, HE, UHE, LPHR*	LEHR	LEHR	LEHR	SMARTZOOM
Detetctor Motion correction method	Data space correction using Multi Head Registration (MHR) data	Image space compensation using optical motion tracking for each detector in 6D	Image space compensation using optical motion tracking for each detector in 6D	Image space compensation using optical motion tracking for each detector in 6D	Image space compensation using optical motion tracking for each detector in 6D
Rotation model	2D	3D	3D	3D	3D
Detector motion characterization	N/A	Adaptive system specific measured 4x4 Gantry Deflection Matrix	Adaptive system specific measured 4x4 Gantry Deflection Matrix	Adaptive system specific measured 4x4 Gantry Deflection Matrix	Class Standard for collimator & configuration measured 4x4 Gantry Deflection Matrix
Sensitivity	N/A	Default Sensitivity Calibration	Default or System specific sensitivity calibration	System specific sensitivity calibration	N/A
Calibration Source	N/A	N/A	^{99m}Tc or ^{57}Co Calibrated Sensitivty Source (CSS)	^{99m}Tc or ^{57}Co Calibrated Sensitivty Source (CSS)	N/A
Uniformity	N/A	Uniformity Correction	Uniformity Correction	Uniformity Correction	Uniformity Correction
Radius-of-Rotation	Encoders for each detector	Encoders for each detector	Encoders for each detector	Encoders for each detector	Encoders for each detector
Reconstruction method	OSEM (Ordered Subset Expectation	OSCGM Ordered Subset Conjugate	OSCGM Ordered Subset Conjugate	OSCGM Ordered Subset Conjugate	OSCGM Ordered Subset Conjugate
Optimization Method	Expectation Maximization (EM)	Pre conditioned Conjugate Gradient	Pre conditioned Conjugate Gradient	Pre conditioned Conjugate Gradient	Pre conditioned Conjugate Gradient
Merit Function	Maximum Likelihood (ML)	Mighell's χ_γ^2	Mighell's χ_γ^2	Mighell's χ_γ^2	Mighell's χ_γ^2
Matrix Size	128 (default), 256 (optional)	128 (optional), 256 (default)	256	128 (optional), 256 (default)	128
Frame Of Reference	SPECT	CT	CT	CT	SPECT
Data Corrections	Nal, Energy&Lineraity (ZLC), Uniformity, MHR	Nal, ZLC	Nal, ZLC	Nal, ZLC	Nal, ZLC
Dicom Input Type	Tomo	Tomo	Tomo	Tomo	Tomo

Figure 1: *Comparison of our iterative reconstruction solutions Flash3D, xSPECT platform and IQ•SPECT available on Symbia Intevo. The color coding indicates either common components or highlights key features of the solution. The colors indicate common as well as specific components of the reconstruction technologies. For instance, xSPECT (orange) is a foundation platform, and thus its components are also present in xSPECT Bone (green) and xSPECT Quant (blue). The latter two have specific additional components highlighted with the respective color. IQ•SPECT (light red) has some specific components which are variants of xSPECT.*

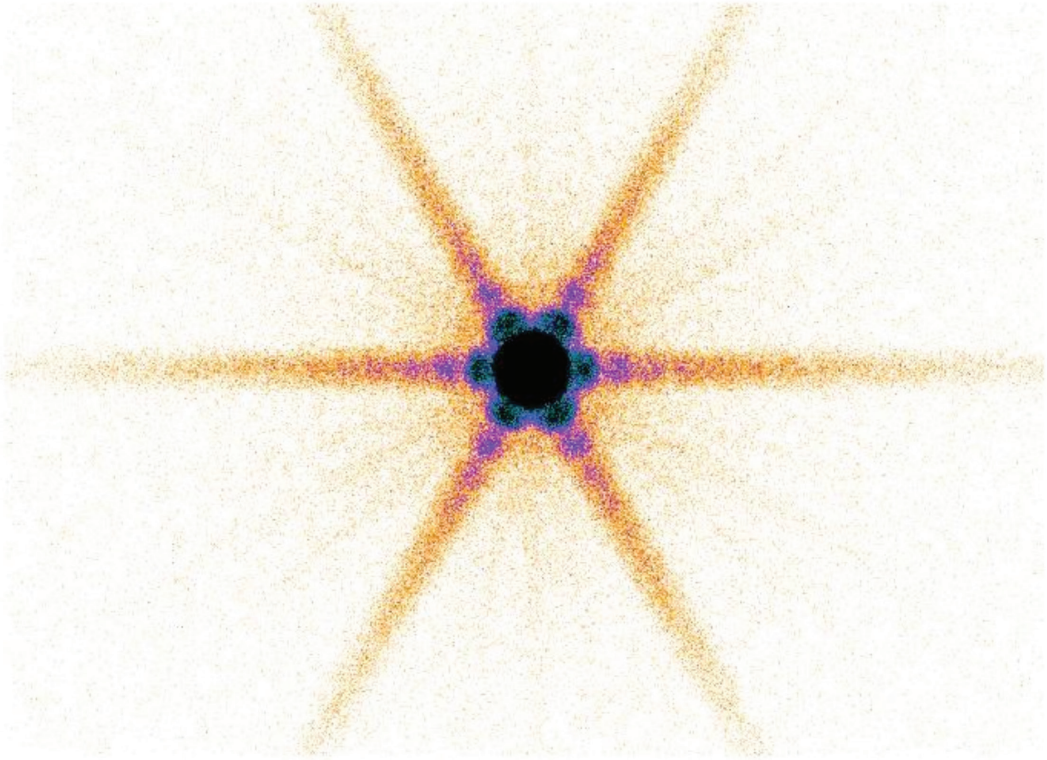

Figure 2: *Measured PSRF of a ^{99m}Tc point source for a Siemens AUTOFORM LEHR collimator stretching over the entire detector FOV and at varying distances. This data is used to construct the measured PSRF and then used inside the xSPECT reconstruction.*

xSPECT reconstruction is very similar to the IQ•SPECT reconstruction method[22], albeit with a few key differences that will be discussed below. Fundamentally, xSPECT operates in the CT Frame-of-Reference (FOR), whereas IQ•SPECT operates in the SPECT FOR. In the IQ•SPECT reconstruction, we rely on the geometric design of the tapered hexagonal holes of the **SMART**ZOOM collimator to compute the collimator's point response function. This is then convolved with the intrinsic resolution represented by a Gaussian to yield a geometric PSRF. For the xSPECT system model, however, we have measured the 3D PSRF of our AUTOFORM® LEHR collimator (Figure 2) over the entire FOV and the entire possible imaging range at the center of the FOV. The translational invariance of the PSRF of the AUTOFORM LEHR has been verified by measurements, justifying the central measurement location only. The angulation error is ±0.05° (RMS) and is highly reproducible for our in-house manufactured AUTOFORM LEHR collimators, as tested over many collimator samples. We can thus have a class standard measurement.

As mentioned above, one key difference between xSPECT and Flash3D (OSEM3D) is the former's faster convergence speed for extended sources (quadratic for CG versus log-linear for MLEM), providing faster resolution and emission recovery at the expense of accelerated noise accumulation. As a result, the number of necessary updates in CG will generally be lower than those for an OSEM3D reconstruction. Our research indicates that the update ratio between EM:CG = 4:1, i.e., 196 EM updates correspond to 48 CG updates, where noise and resolution are essentially equal. This is also consistent with Tsui[18]. The noise structure of xSPECT differs from Flash3D as it appears more mottled, particularly in soft tissue and other background regions. This difference was noted by clinical readers, but it was judged not to be clinically relevant (Figure 25).

A detailed discussion of the characteristics of our xSPECT method at various updates, count levels and for various objects and contrasts is outside the scope of this overview summary, but will be presented in a subsequent white paper. As a default, we recommend 48 updates and 1 subset, but the number of updates must be reduced for very low count data.

The impact of improvements in the image formation model, as well as the use of a different reconstruction engine, can be visualized in the reconstructions of phantom data. The images** below (Figure 3, Figure 4) of the Data Spectrum Cylinder phantom with hot and cold rod inserts allow for a comparison between a Flash3D and an xSPECT reconstruction. For xSPECT, the cold rods have a higher contrast, and the hot rods are also better resolved, yet the background seems a bit noisier than for Flash3D at typical update parameters.

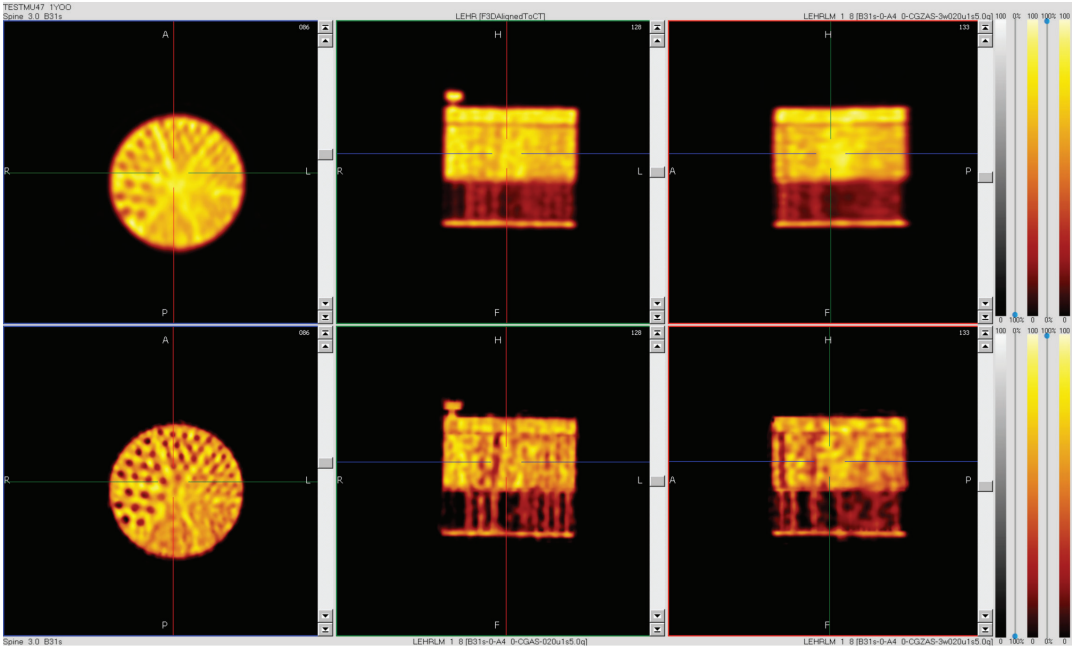

Figure 3: *Data Spectrum, Deluxe hot and cold rod inserts (cold). Top row: Flash3D. Bottom row: xSPECT reconstruction below. Both methods are attenuation and scatter corrected (display from research workstation).*

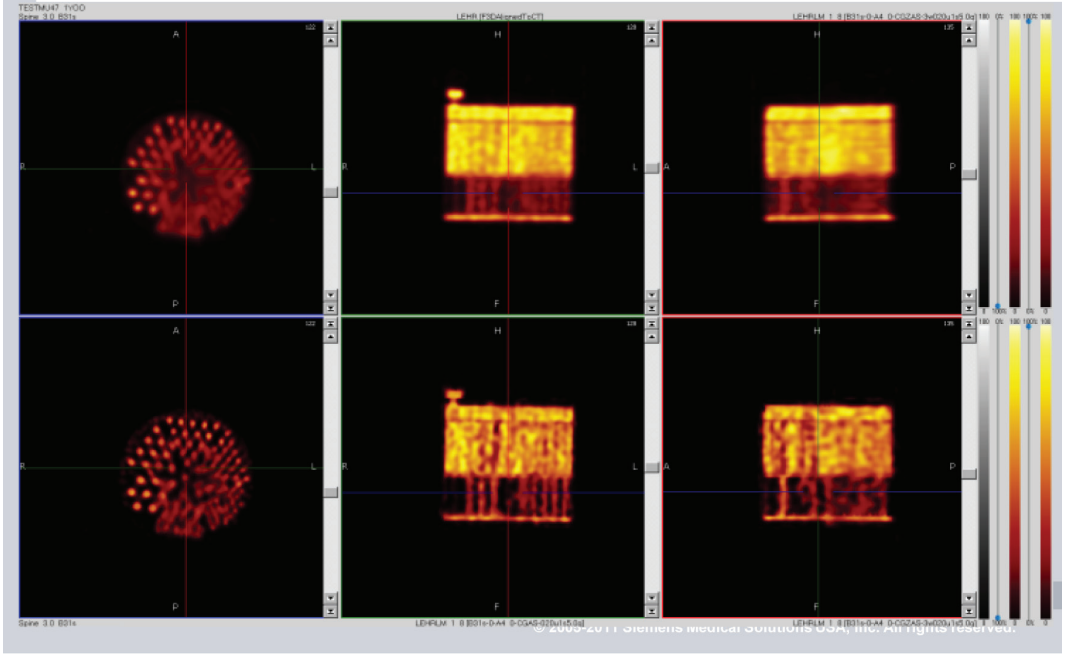

Figure 4: *Data Spectrum, Deluxe hot and cold rod inserts (hot). Top row: Flash3D. Bottom row: xSPECT reconstruction below. Both methods are attenuation and scatter corrected (display from research workstation).*

** *The images are displayed using our research Clinical Visualization Research Tool (CVRT), which allows for three-way fusion, hence the pair of blending bars with three color table selectors on the right side of the display. The CVRT also contains basic VOI analysis tools and is only available for our research collaboration partners.*

The First Application: xSPECT Bone

The concept of context-sensitive reconstruction

A new reconstruction method was developed by Siemens and applied to ^{99m}Tc diphosphonate Bone SPECT studies using the xSPECT engine described above as a foundation. An overview of the typical image quality currently available in bone imaging is given by Evan-Sapir.[23] We seek to improve on the image quality of SPECT using the available information from the CT in tandem with the knowledge that disphosphonate is taken up by bone tissues experiencing high rates of bone turnover.[24] Thus, it is reasonable to define zones that distinguish and delineate bone from non-bone in the reconstruction.

In the case of xSPECT Bone, CT data is not only used for attenuation correction, but also to delineate tissue boundaries. This is achieved by first converting the transaxial CT data to a linear attenuation map maintaining the CT data structure and resolution.[25] Based on the linear attenuation coefficients at 140 keV, five tissue classes ("zones")*** are defined: air and lung, adipose, soft tissue, soft bone and cortical bone. The transition between these zones is smooth, representing a soft segmentation. All reconstruction voxels thus are labeled with an index that determines the zone class. Voxels within a particular zone class are forward projected as a group, but remain distinct from other zone classes and are handled separately in projection space. The basic iterative reconstruction method (xSPECT technology) is described above, and the following is a description detailing the incorporation of application-specific contextual information.

Implementing extra-modal information into the reconstruction

The process begins by adapting the forward projection to the multizone situation and applying the forward projection operation to each zone's specific image object separately. The zonal forward projections, therefore, consider the contribution of each zone to the image model separately. Specifically, the zonal forward projections use the zone-masks $z_\alpha^{(n)}$ to define the class-specific contribution. Any stray values that the zonal image object may have received at object points outside its specific zone due to the update operation are multiplied by zero or other value according to the value of the corresponding zone-function at that point. Thus, each of the resulting zonal data models $m_i^{(n)}$ can be described by

$$m_i^{(n)} = \sum_\alpha H_{i\alpha} z_\alpha^{(n)} I_\alpha^{(n)} \qquad \forall n \,. \tag{8}$$

The total data model m_i is represented by a sum of the zonal data models, plus a scatter estimate:

$$m_i = \sum_n m_i^{(n)} + s_i \,. \tag{9}$$

The non-negative scaling factors can influence the data model via the scaling of the zonal image objects $I_\alpha^{(n)}$ as follows:

$$I_\alpha^{(n)} \to c_n I_\alpha^{(n)} \qquad c_n \geq 0 \qquad \forall n \tag{10}$$

This leads to a corresponding scaling of the zonal data models $m_i^{(n)}$:

$$m_i^{(n)} \to c_n m_i^{(n)} \qquad \forall n \,. \tag{11}$$

The scaled total data model mscaled m_i^{scaled}, as generated by the zonal forward projection including scaling and scattering correction, is given by modifying the sum in $m_i = \sum_n m_i^{(n)} + s_i$, as follows:

$$m_i^{scaled} = \sum_n c_n m_i^{(n)} + s_i \,. \tag{12}$$

The merit function is optimized for the scaling factors c_n, which, in general, is an optimization of only a few parameters (e.g., the N scaling factors c_n). The output of the zonal renormalization process includes an optimized scaling factor c'_n for each zonal image object $I_\alpha^{(n)}$.

Generation of the zone map for the ^{99m}Tc Di-Phosphonate application

The "zone map" is the result of a voxel-by-voxel conversion of the CT image to the discrete tissue classes. In our work, we determined that five tissue classes: cortical bone, soft bone, soft tissue, adipose and lung tissue yield the best clinical impression. The transition from one tissue class to another tissue class is smooth and given by a polynomial of third order, symmetric at the midway point in between the tissue boundaries. The conversion is done via an intermediate step of converting the CT image to a linear attenuation coefficient volume at a fixed reference energy of 140 keV using our patented adaptive HU-to-LAC conversion method. This step is needed to reduce inconsistent zone boundaries, introduced by the inherent variability of the HU determination of bone tissue, which otherwise could impact xSPECT Bone image quality. The reference tissues used are available from Gammex, Inc.

The multi-modal reconstruction algorithm†

1. For each zone, multiply the (single) image by the zonal weights of the voxels to create a zonal image.
2. Forward project the zonal image to create a zonal data model.
3. The combined data model is a linear combination of the zonal data models with coefficients c_n.
4. Set each c_n such that χ_γ^2 is minimized.
5. If a c_n <0, set the most negative one to zero and repeat step 4 keeping it fixed at zero. Continue until there are no negative coefficients. (This step is what prevents the use of the method in conjunction with EM.)
6. Set the data model to the linear combination with the c_n determined in steps 4 and 5.

*** *Zones are an example of Extra-Modal Information ("EMI") extracted from the CT.*
† *Patents pending. US Patents: 8,675,936; 8,577,103; 6,950,494*

Figure 5: *Multi-modal reconstruction with zonal weights.*

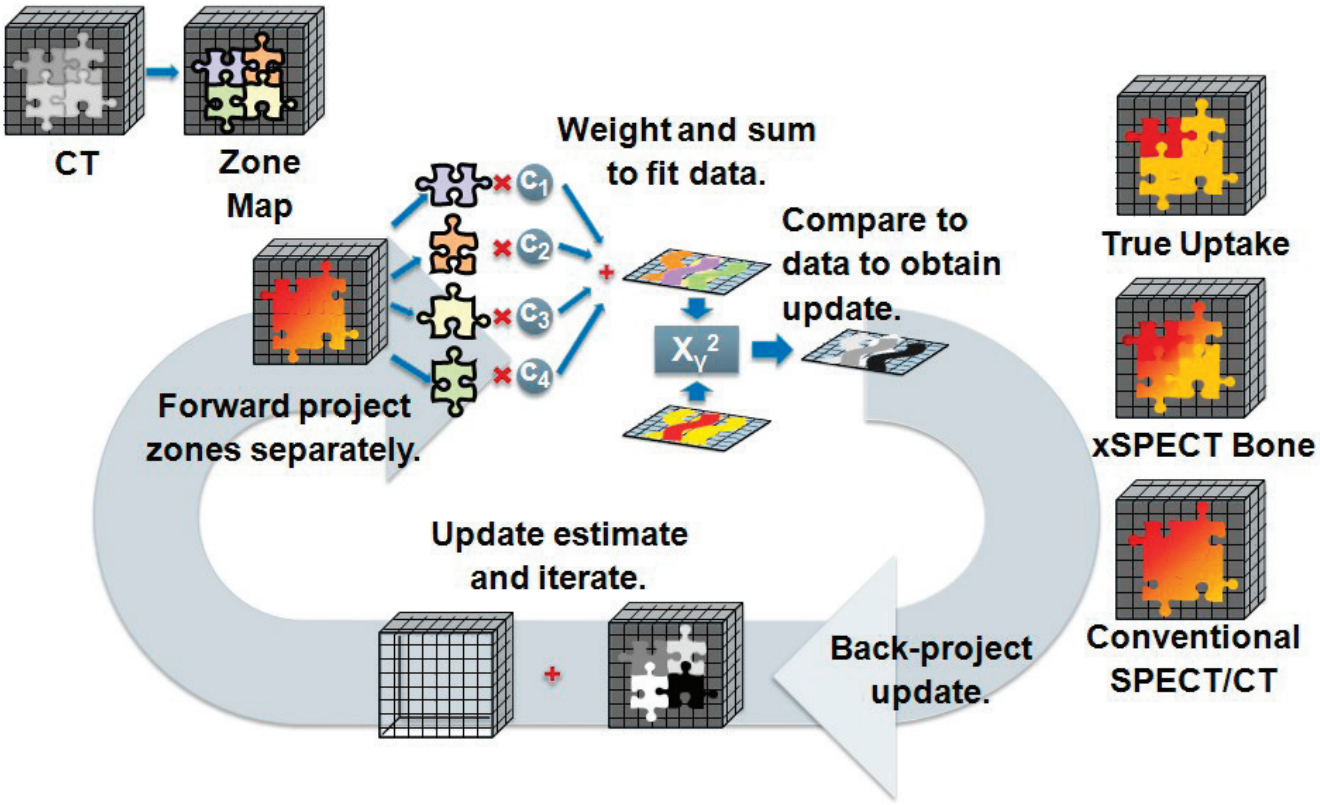

7. Reset the image to a linear combination of the zonal images with the same c_n.
8. The image and the data model have now been changed consistently (due to the linearity of the forward projection). Discard the zonal images, data models and zonal coefficients c_n.
9. Compute the conjugate gradient, minimize and update the image using the back projection without regard to zones.

If the stopping criterion has not been reached, repeat steps 1-9 for the next update. Otherwise, terminate the reconstruction.

Figure 5 illustrates the concept graphically. As usual, early stopping of the iterations in tandem with post smoothing acts as a type of smoothness regularization. Simple post smoothing would, however, blur the zonal boundaries. Thus, we employ an edge-preserving filter, which maintains crisp zonal boundaries and only smooths within them. Each zone can thus be smoothed independently. We chose a 3D Gaussian and smooth bone zones at half the FWHM of the non-bone zones. In Figure 6, we show that the CT reconstructed data is used without degradation for both the attenuation map and the zonal map.

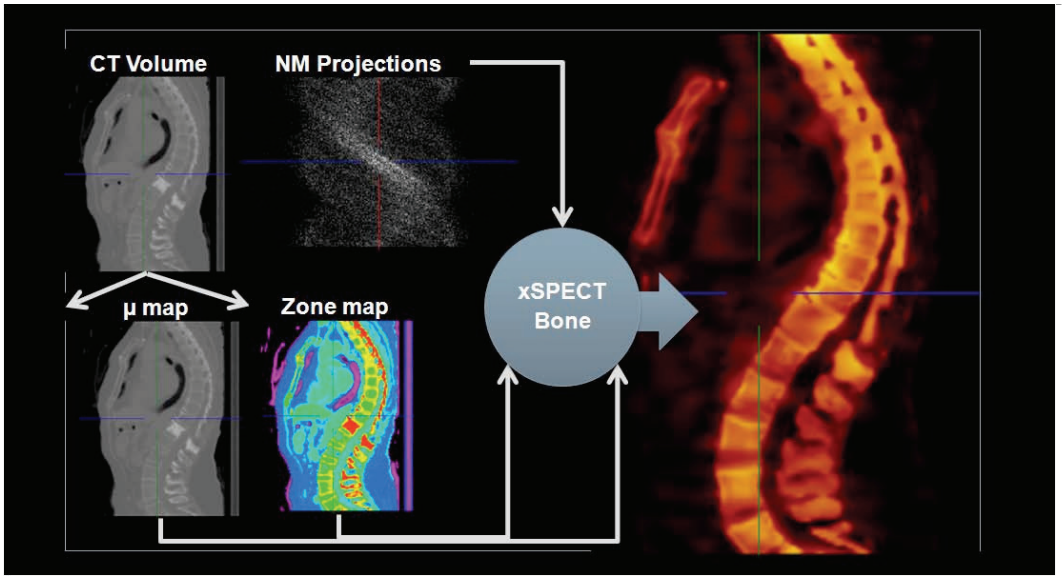

Figure 6: *xSPECT Bone. Use of CT data to generate an attenuation map, as well as a zone map (display from research workstation).*

Date courtesy of University of Minnesota, Minneapolis, Minnesota, USA.

Figure 7: *Null experiment using Data Spectrum sphere inserts: Top row: Flash3D (Sphere : Cylinder = 60:63 contrast) . Bottom row: CT images. Contrast adjusted to 0.194 cm^{-1} (display from research workstation).*

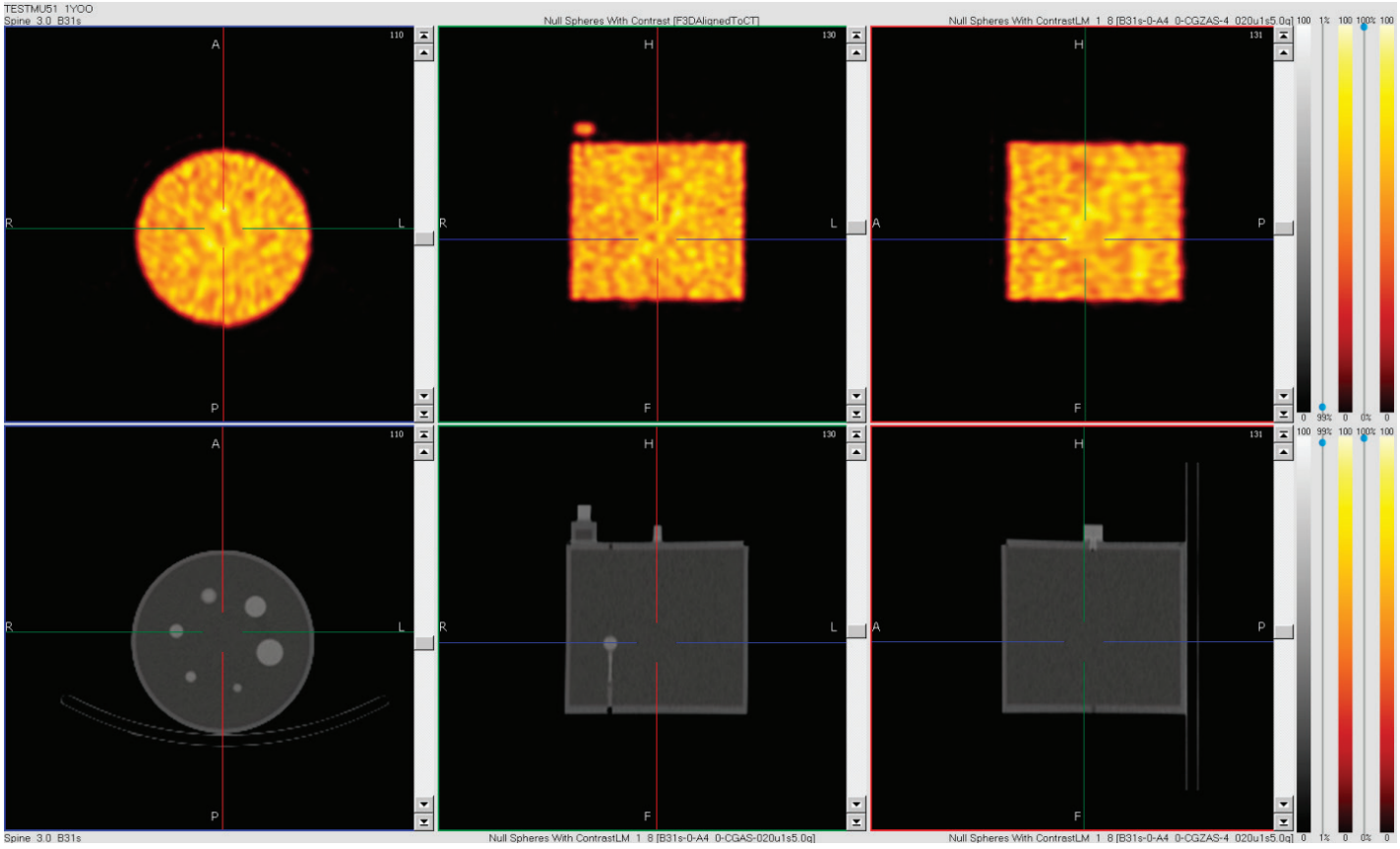

Please note that this approach is different from using a Bayesian model that incorporates anatomical priors derived from a CT in the reconstruction of functional emission imaging.[26-30] For reconstruction algorithms employing a Maximization of the A Posteriori probability (MAP) approach, one incorporates a prior distribution to produce an *a posteriori* probability distribution conditioned on the data. xSPECT neither assigns probabilities, nor does it make assumptions regarding where and how much the activity concentration should be.

Another approach by Calvini uses the CG method to enhance SPECT data by MR solving a "shifted" problem, whereby the MR signal of low spatial frequency is replaced by the SPECT projector-backprojector operator.[31] This is also different from the method employed by xSPECT, which is driven by the emission data and whose solution is consistent with this data.

Testing the concept: probing the obvious pitfalls with phantoms

Examples of the image quality can be assessed in the following figures, which demonstrate a few key differences compared to conventional current state-of-the-art iterative SPECT reconstruction (Flash3D).[7]

Using a set of null-experiments, we can demonstrate that the context based xSPECT reconstruction:

a. does not show significant false correlations between uptake and HU values†;
b. does not spread or shift the activity centers for deep seated lesions.

In one case, the activity within two different zones (differentiated by different densities) is essentially the same, and in the other case the density concentration is the same, but the activity concentration is different.

We use, for all our tests described here, phantoms from Data Spectrum, Hillsborough, NC, USA; please refer to the vendor for detailed product information.

For the purpose of testing (a) above, we filled the set of six hollow spheres (0.5 ml- 16ml) in a warm background (flangeless cylinder) with following quantitative loading at the start of the scan (Figure 7): Cylinder - 63 kBq/ml, and Sphere-set - 60 kBq/ml, yielding a 60:63 contrast. CT contrast was added to spheres so that the inner LAC-values were 0.194 cm^{-1}.

† *It should be noted that such a correlation is dependent on the volume of interest and a host of other variables.*

In Figure 8 we see the results of this experiment, with Flash3D on the top row and the xSPECT context reconstruction on the bottom. The Flash3D reconstruction appears as a more or less homogeneous phantom due to the true low contrast between spheres and background. Similarly, in the xSPECT case, the experiment shows (statistically) the same uptake in the spheres as in the background. A trace of the sphere shell is visible, mainly due to the fact that the forward projection of voxels inside the spheres and outside the spheres is done separately.

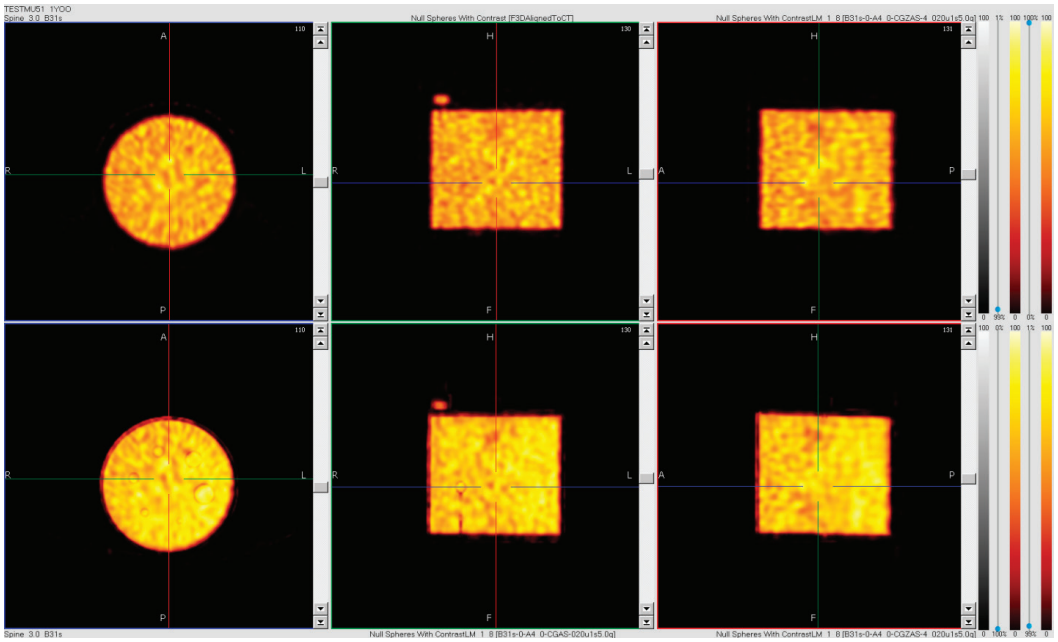

Figure 8: *Null experiment using Data Spectrum's hollow sphere set: Top row: Flash3D (Sphere: Cylinder = 60:63 contrast). Bottom row: xSPECT's reconstruction with zonal information (context). A trace of the boundary region is still visible, but the contrast is reproduced, and the null experiment passed (display from research workstation).*

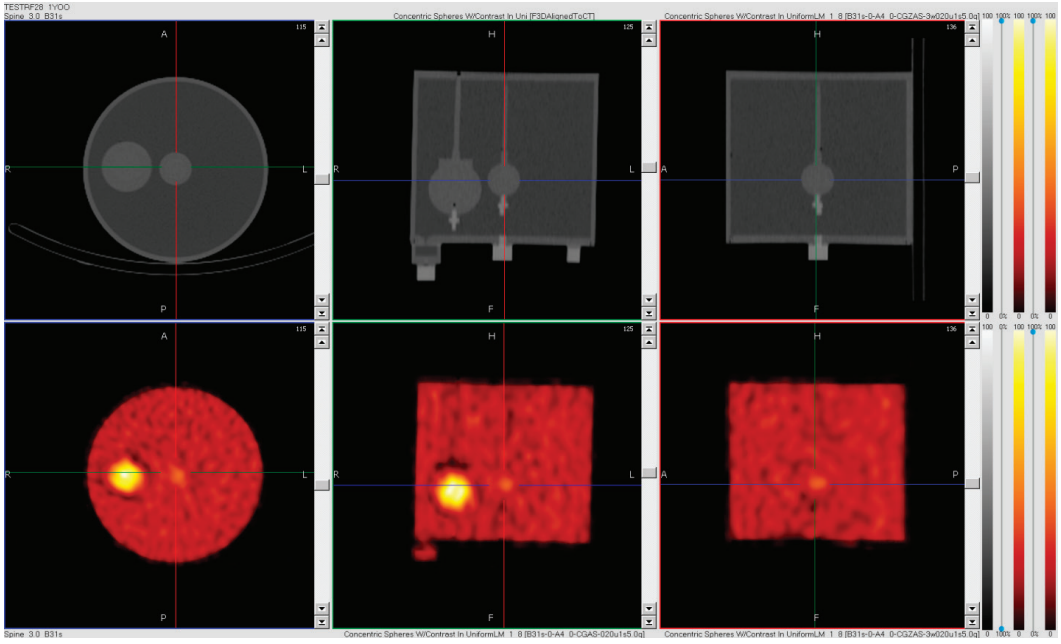

Figure 9: *Concentric spheres of 2 different sizes inside a cylinder (Data Spectrum). Top row: CT. Bottom row: xSPECT's reconstruction without zonal information. The lack of activity at the base of the large sphere is visible, as that base is solid plastic. Both methods are attenuation and scatter corrected (display from research workstation).*

For the second null experiment (Figure 9, Figure 10, Figure 11), we set up two sets of concentric spheres with the same density contrast, but loaded the inner sphere such that it had a higher activity concentration than the shell sphere:

1. Cylinder: 58.9 kBq/ml.
2. Large sphere shell (70 cc volume): 57.7 kBq/ml and core (20 cc volume): 228.5 kBq/ml.
3. Small sphere shell (volume 12 cc): 57.7 kBq/ml and core (5.5 cc volume): 121 kBq/ml.
4. CT contrast added to water inside spheres such that their mu-values were 0.172 cm^{-1}, same as acrylic plastic.

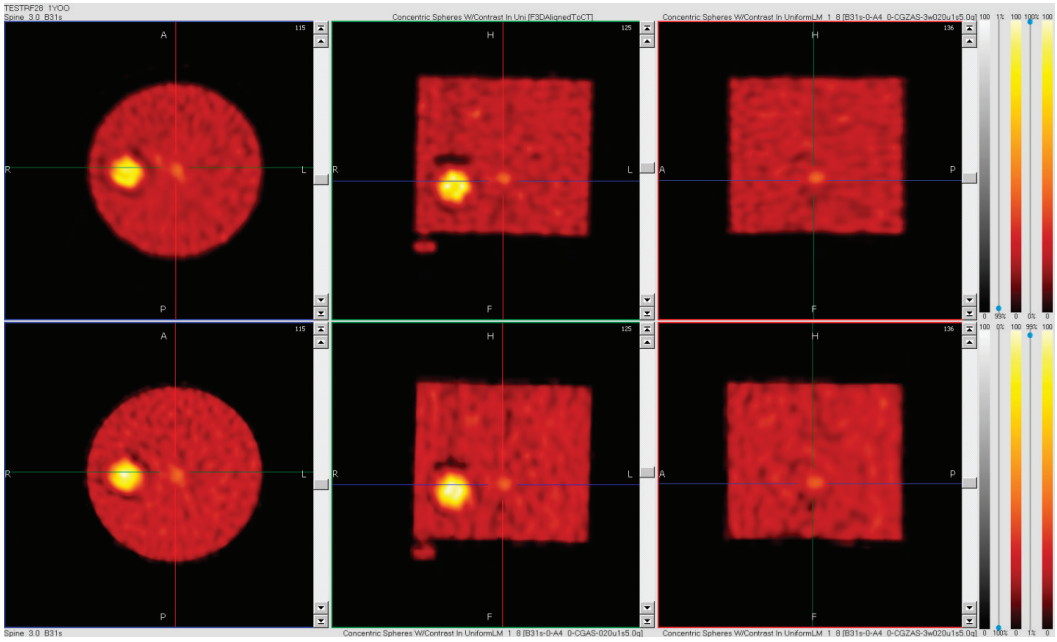

Figure 10: *Concentric spheres of 2 different sizes inside a cylinder (Data Spectrum). Top row: Flash3D. Bottom row: xSPECT's reconstruction without zonal information. The lack of activity at the base of the large sphere is visible, as that base is solid plastic. Both methods are attenuation and scatter corrected (display from research workstation).*

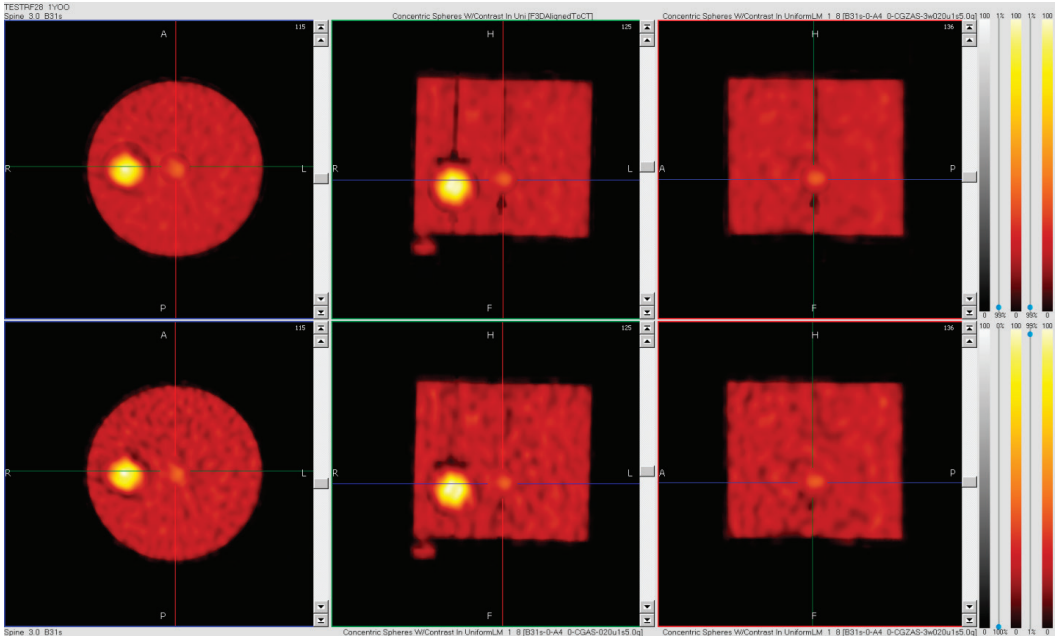

Figure 11: *Concentric spheres of 2 different sizes inside a cylinder (Data Spectrum). Top row: xSPECT reconstruction with zonal information (context). Bottom row: xSPECT's reconstruction without zonal information. The lack of activity at the base of the large sphere is visible, as that base is solid plastic. Both methods are attenuation and scatter corrected (display from research workstation).*

Figure 12 and Figure 13 show Data Spectrum's hot and cold rod insert (Deluxe) using the xSPECT reconstruction with context information compared to without.

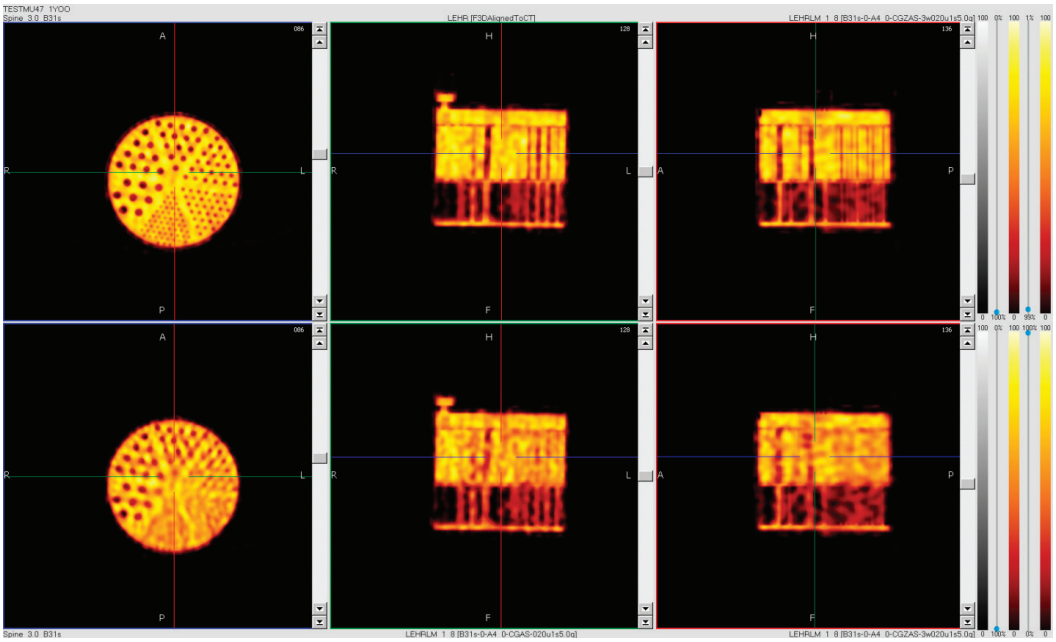

Figure 12: *Data Spectrum, Deluxe hot and cold rod inserts (cold). Top row: xSPECT reconstruction zonal information. Bottom row: xSPECT's reconstruction without zonal information. The zones are adjusted to separate plastic from water. Both methods are attenuation and scatter corrected (display from research workstation).*

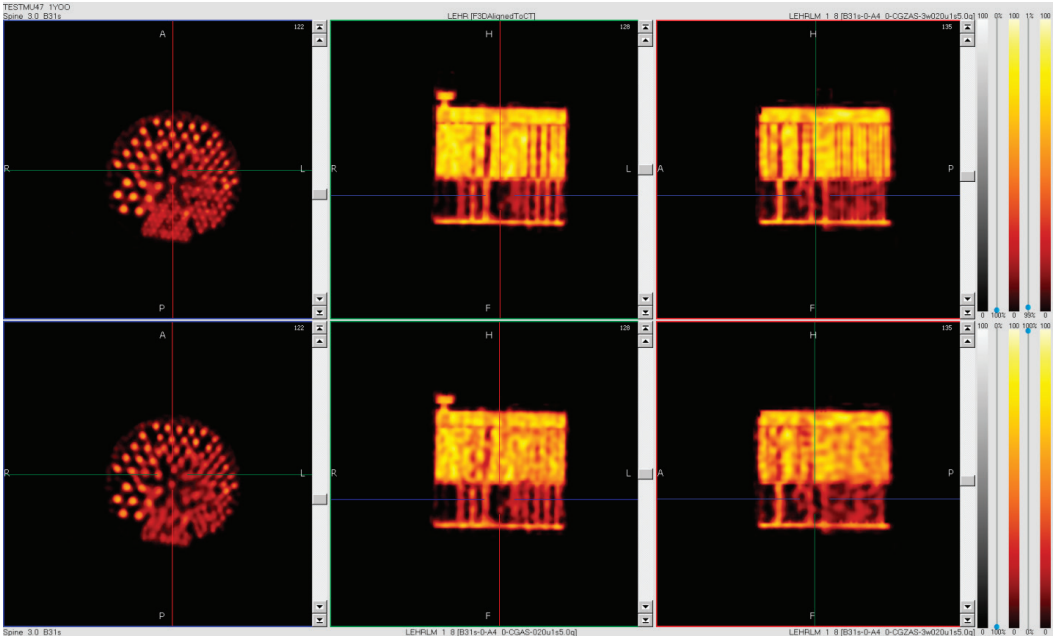

Figure 13: *Data Spectrum, Deluxe hot and cold rod inserts (hot). Top row: xSPECT reconstruction zonal information. Bottom row: xSPECT's reconstruction without zonal information. Both methods are attenuation and scatter corrected (display from research workstation).*

Testing the concept: clinical feasibility

Figure 14 and Figure 15 show a clinical example to demonstrate the image quality on patient data. The female patient with breast carcinoma was referred to a bone scan and worked up under the site's clinical protocol. This patient was injected with 925 MBq of ^{99m}Tc-MDP, and imaged about 3h later in a 360 degree SPECT scan with 120 views. The scan was performed on a Symbia T6 using the VA63A software version*†. VA63A is able to deliver both clinical framed projections, as well as list mode data for research purposes.

The clinical data was processed with clinically used methods only, and the list mode data with a prototype of xSPECT Bone. Due to site regulations and IRB requirements, we maintain a strict separation of clinical and research data. The data is anonymized, and sent to an Advanced Research Reconstruction Computer (ARC) on-site, which is also linked to a dedicated site "clone" ARC at the factory. Only anonymized data is transferred from the site to the factory, the site maintains the key, as well as back-up.

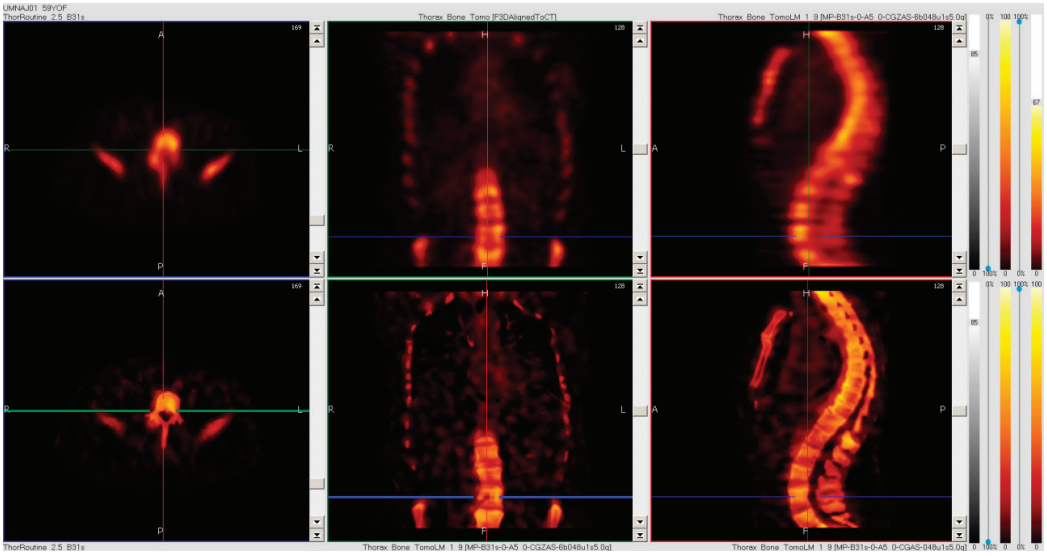

Figure 14: *Top row: Flash3D reconstruction using attenuation and scatter correction. Bottom row: xSPECT Bone of the same data. (display from research workstation)*

Data courtesy of University of Minnesota, Minneapolis, Minnesota, USA.

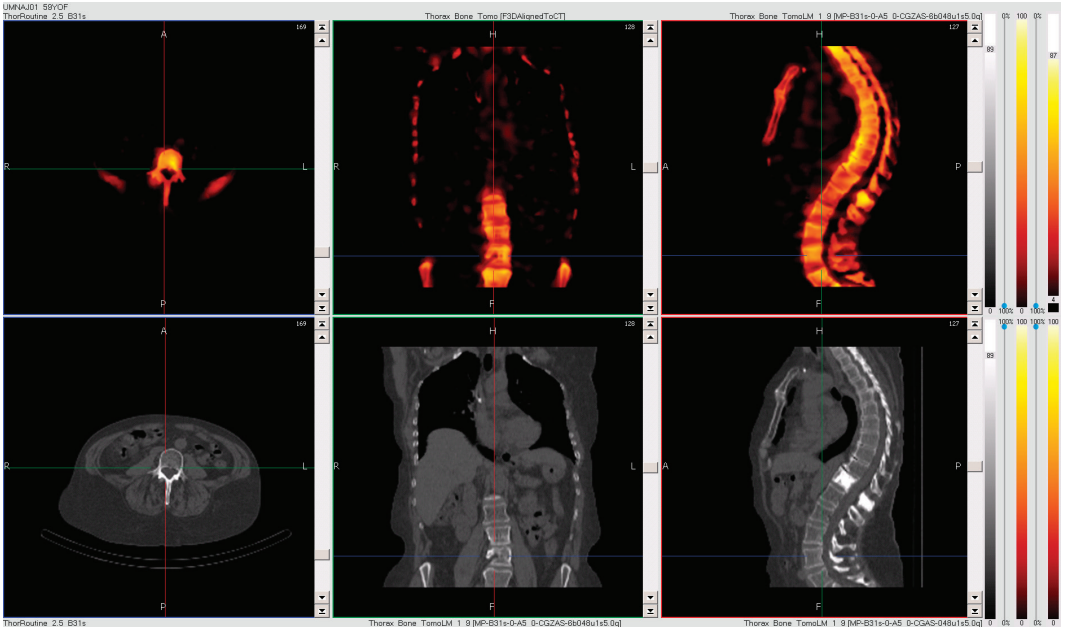

Figure 15: *Top row: Context based reconstruction xSPECT Bone. Bottom row: CT image. (display from research workstation)*

Data courtesy of University of Minnesota, Minneapolis, Minnesota, USA.

**† VA63A is only for clinical collaborators, and not for sale.*

Figure 16 and Figure 17 show a further clinical example. A 74-year-old male with primary indication of adenocarcinoma of the prostate was injected with 925 MBq of ^{99m}Tc-MDP, and worked-up under the site's clinical protocol. The scan was performed on a Symbia T16 with the same software described above (VA63A). As with the previous example, the clinical data was processed with existing methods (i.e., Flash3D with CT and attenuation correction and scatter correction), while the list mode data was reconstructed using a prototype of xSPECT Bone (Data courtesy of Johns Hopkins University, Baltimore, Maryland, USA).

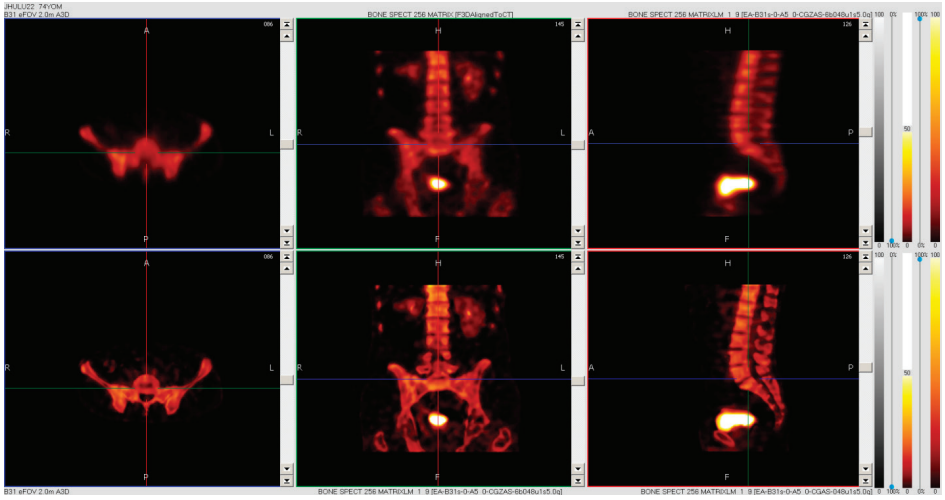

Figure 16: *Top row: Flash3D reconstruction using attenuation and scatter correction. Bottom Row: xSPECT Bone reconstruction of the same data. (display from research workstation)*

Data courtesy of Johns Hopkins University, Baltimore, Maryland, USA.

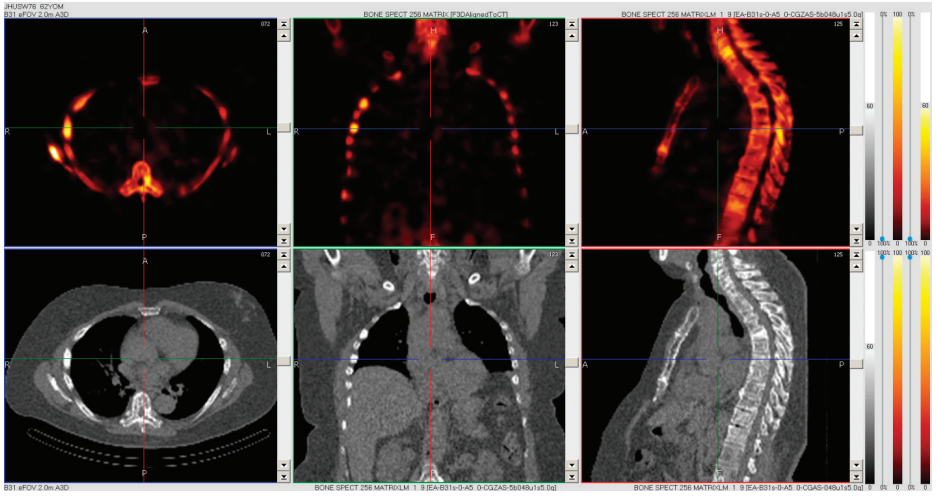

Figure 17: *Top row: Context based reconstruction xSPECT Bone. Bottom row: CT image. (display from research workstation)*

Data courtesy of Johns Hopkins University, Baltimore, Maryland, USA.

The image quality is improved in the xSPECT Bone images. In particular, resolution appears higher. However, it has to be stressed that this is a multi-modal resolution image owing to the truly multi-modal nature of the reconstruction. The resolution is not determined by a single modality, but is an amalgamation of the resolutions of both. Boundaries of different tissue classes are well resolved, as they are delineated with the sharp resolution of the CT and exhibit better resolution than that offered by the nuclear PSRF alone. The interior of each tissue class, however, shows a resolution similar to conventional nuclear reconstruction.

The aforementioned edge-preserving post-smoothing method helps maintain these boundary characteristics even after post smoothing by handling each zone separately. In this case, bone zones are smoothed with a 5mm FWHM 3D Gaussian, whereas all other zones (i.e., soft tissue) are smoothed with 10 mm, roughly corresponding to the matched filter of the PSRF at the average radius-of-rotation and is equivalent to the classical choice of post-smoothing kernel size.

Evaluations of xSPECT Bone

It has been shown that SPECT fused with CT has improved sensitivity, equal or improved specificity for differentiation of benign and malignant focal bone lesions in the axial skeleton with 82% and 94% for planar scintigraphy, 91% and 94% for SPECT, 100% and 100% for SPECT fused with CT.[32] Even-Sapir et al. shows an improvement of sensitivity, specificity, negative and positive predictive values of SPECT/CT over planar imaging in high-risk prostate carcinoma patients.[33] Despite these high clinical values of SPECT/CT, there is still improvement possible, and we propose the use of context-based reconstruction to further improve the clinical application.

The new method described above was refined over several years based on feedback from various luminary sites. The readers took advantage of their respective patient populations and assessed image quality across various software updates as well as preferences for the parameter ranges used when fine-tuning the reconstruction. Throughout this collaboration, we used a 2-alternate force choice method and designed a research tool to examine the comparative image evaluation. (In some cases, we allow for reporting a tie, as decision times to pick one or the other became too lengthy.) A brief summary of the method and results are presented at the SNMMI 2013.[34] Ultimately, these results are the basis for the final version of the reconstruction method and recommended parameter ranges in the product.

Concordance evaluation

During the more recent stages of the collaboration, we designed experiments to evaluate potential clinical benefits. The study was designed for two phases: pilot and full evaluation phase. The goal of the pilot study is to help in the design of the full evaluation and to assess image quality and clinical acceptance of xSPECT Bone among experienced readers relative to Flash3D (Flash3D), which is currently in clinical use. The full evaluation commenced in the summer of 2013, and results will be available once completed.

The goal of the pilot study was to probe the three aims listed below:

Aim 1: Concordance among readers regarding general impression of disease.
Aim 2: Quantify differences in image quality of Flash3D and xSPECT Bone.
Aim 3: Lesion-based scoring for statistical analysis of reader concordance

We present here only a brief summary of Aim 2:

All data were acquired on Symbia T series in dual mode (using VA63A to provide clinical and NM list mode data) setting under approved Institution Review Board (IRB) at the participating sites. From a pool of patient data that was not used in any prior research assessment, we obtained patients who had undergone both thorax and abdomen SPECT exams, resulting in 9 patients (3 male) from 4 different sites (2 sites in the US and 2 sites in Germany), each with slightly different protocols and patient populations. The data ranged in total counts from 4.8 Mc to 11 Mc for the thorax scan and from 2.5 Mc to 11 Mc for the abdomen scan. The injected tracer was either MDP (US) or DPD (Germany).

SPECT images of the chest were reconstructed with Flash3D, and the prototype of xSPECT Bone, both to obtain best possible image quality. Both methods included 3D resolution recovery (albeit with different PSRF models), attenuation and scatter corrections. In addition, xSPECT Bone incorporated CT information to delineate tissue boundaries during image reconstruction. The Flash3D and xSPECT images were presented to ten experienced readers in random order. Both SPECT scans were displayed together with the corresponding whole body planar and MIP (Maximum Intensity Projection) images.

The readers were asked to respond to 13 questions (Figure 18) on a 5 point scale, where a lower number is more favorable from the patient point of view. The questions Q1-Q6, Q12, and Q13 probe aspects relating to image quality: noise w.r.t. diagnostic importance, resolution w.r.t. diagnostic importance, diagnostic utility, and clinical acceptance. Questions Q8-Q11 prompt the readers to subjectively assess their impressions ("gut feel") on clinical benefits, such as specificity.

AIM2:	Quantify differences in image quality of F3D and A3D	Scores
Question 1:	Please rate your general impression of the noise:	1: minimal–5: severe (not useable for a read);
Question 2:	Please rate your general impression of the diagnostic importance of the noise	1: insignificant–5: significant (not useable for a read);
Question 3:	Please rate your general impression of the image resolution?	1: excellent–5: poor (not useable for a read);
Question 4:	Please rate your general impression of the diagnostic importance of the image resolution	1: significant–5: insignificant;
Question 5:	How many distinct artifact classes do you see?	1: 0, 2: 1-2,3: 3-5,4: 6-9,5: 10+;
Question 6:	Please rate your general impression of the diagnostic importance of these artifact classes:	1: irrelevant–5: relevant;
Question 7:	How many artifact classes do you see that are diagnostically disturbing or causing concern?	1: 0, 2: 1-2,3: 3-5,4: 6-9,5: 10+;
Question 8:	In your estimate, please rate your impression of increase in lesion detection specificity compared to Planar/Wholebody:	1: very significant–5: insignificant; 6: Decrease
Question 9:	In your estimate, please rate your impression of increase in lesion detection sensitivity compared to Planar/Wholebody:	1: very significant–5: insignificant; 6: Decrease
Question 10:	In your estimate, please rate your impression of increase in lesion conspicuity compared to Planar/Wholebody:	1: very significant–5: insignificant; 6: Decrease
Question 11:	In your estimate, please rate your impression of increase in your diagnostic confidence compared to Planar/Wholebody:	1: very significant–5: insignificant; 6: Decrease
Question 12:	Please rate your impression of diagnostic utility of the image as presented & compared to your clinical practice:	1: High–5: Minimal; 6: Detrimental
Question 13:	SPECT images only: Overall, do you accept the image and would you use it in your clinical practice?	1: strong yes, 2:yes, 3:equivocal, 4:no, 5:strong no

Figure 18: *Questions and scores of the AIM2 image evaluation. Q1-Q4, Q12,Q13 are highlighted and its results presented below.*

First, we analyze the responses by averaging over the ten readers using a Bland-Altman analysis. Then we pairwise compare the responses of all readers, using an intra-class correlation coefficient (ICC) of the concordance performed according to Shrout et al.[35] for all questions. Please note that on the 5 point scale, a smaller number represents a superior score. Questions 8-12 also allow for a value of 6 to indicate a degradation in image quality.

For Questions 1-4, 12 and 13 (blue gray in Figure 18) we present a Bland-Altman analysis of the scores showing an average improvement for xSPECT Bone of 0.8 compared to Flash3D (Figure 19), with a ΔMedian(M)=0.75, Negative ranks of 46, positive ranks of 8, and Z=5.248, p<0.0001,paired Wilcoxon (W) (Figure 20).

Figure 19: *Bland-Altman Analysis between xSPECT Bone and Flash3D, showing a significant improvement of reader response score over all readers and studies.*

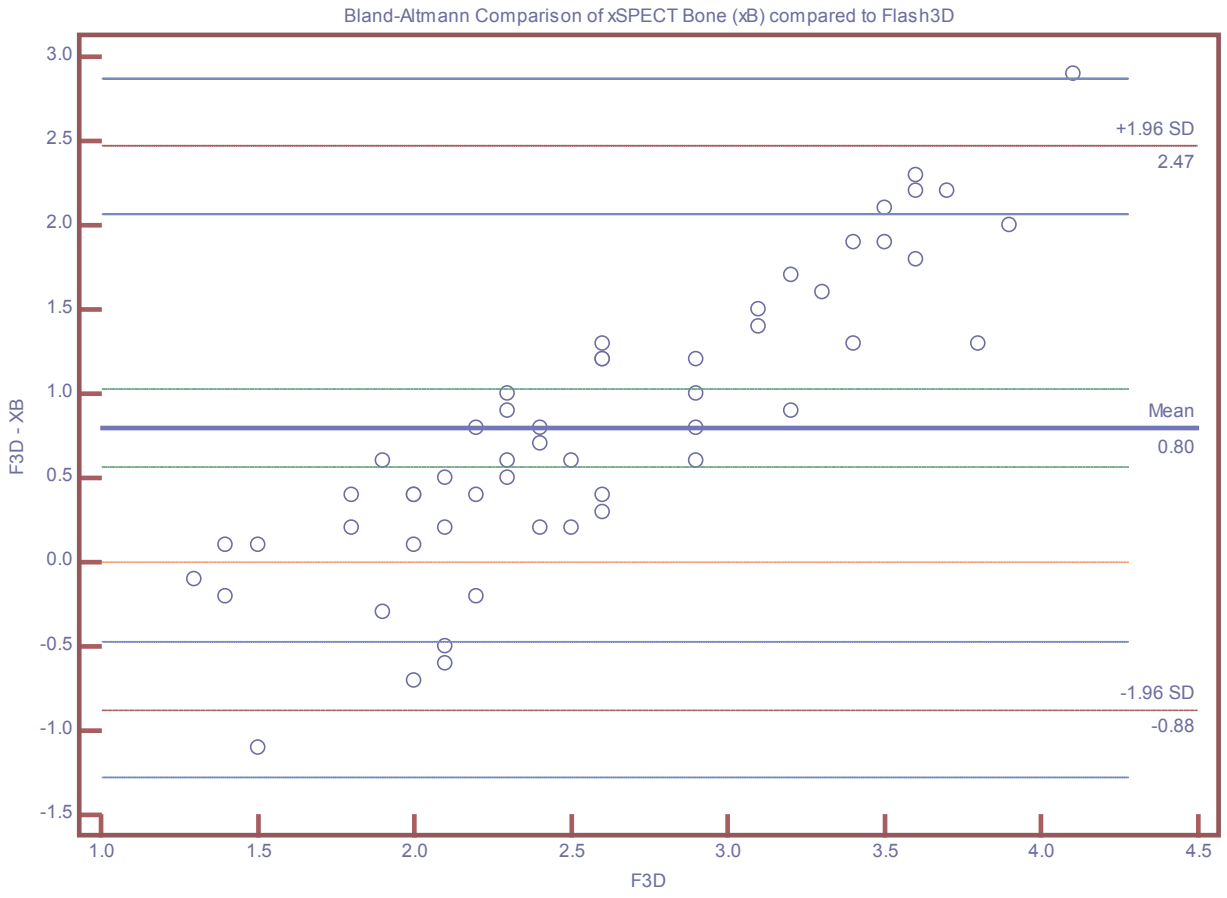

	Wilcoxon (all)			
	Negative Ranks	**Positive Ranks**	**Z**	**p**
	46	**8**	**5.248**	
	F3D	xSPECT Bone	Delta	
N	54	54	0	
Median	2.45	1.7	0.75	
lowest	1.3	1.2		**<0.0001**
highest	4.1	2.7		
95% CI Median min	2.23	1.60		
95% CI Median max	2.80	1.87		

Figure 20: *Summary of the Wilcoxon test of all data of the Chest read.*

xSPECT Bone images were ranked equivalent to or higher than Flash3D images in >85% of the cases. The strongest improvement over Flash3D was observed for the image resolution criterion, with ΔM=2.1, p=0.0039(W) and its corresponding diagnostic importance with ΔM=0.7, p=0.0039(W) (Figure 21). This was followed by diagnostic utility with ΔM=1.3, p=0.0039(W) and image acceptance with ΔM=0.9, p=0.0039(W) (Figure 22) .

In contrast, question 1, assessing the noise in the image, results in a score difference ΔM=04, p=0.7344(W) with 5 negative and 4 positive ranks, and thus is not considered significant.

In Figure 23 and Figure 24 (page 19) we show the results of a Bland-Altman analysis for the average reader first on only the IQ questions, then for all questions. The intra-method comparison (i.e., comparing Flash3D or xSPECT Bone scores against itself for the thorax and abdomen regions) could serve as a "control" to test if the two methods alone perform significantly differently across different anatomical regions. This test resulted in a mean difference of 0.14 (+1.03 -0.74, 95%) and -0.04 (+0.91 -0.98, 95%) between the thorax and abdomen for Flash3D and xSPECT, respectively. This shows that the obtained difference in the mean for the inter-method comparison may indicate that there is indeed a preference for xSPECT Bone, rather than potentially being confounded by a preference for a particular anatomical region.

In the next section, we analyze the responses pair wise and by individual readers and questions.

	Wilcoxon (Resolution, Q3)				Wilcoxon (DxImportance of Q3 finding, Q4)			
	Negative Ranks	**Positive Ranks**	**Z**	**p**	**Negative Ranks**	**Positive Ranks**	**Z**	**p**
	9	**0**			**9**	**0**		
	F3D	xSPECT Bone	Delta		F3D	xSPECT Bone	Delta	
N	9	9	0		9	9	0	
Median	3.6	1.5	2.1		2.4	1.7	0.7	
lowest	3.2	1.2		**0.0039**	2.1	1.3		**0.0039**
highest	4.1	1.9			2.6	2.2		
95% CI Median min	3.41	1.31			2.30	1.43		
95% CI Median max	3.86	1.77			2.60	2.16		

Figure 21: *Summary of the Wilcoxon test of Q3 "Please rate your general impression of the image resolution?" and Q4 "Please rate your general impression of the diagnostic importance of the image resolution".*

	Wilcoxon (DxUtility, Q12)				Wilcoxon (Clinical Acceptance, Q13)			
	Negative Ranks	**Positive Ranks**	**Z**	**p**	**Negative Ranks**	**Positive Ranks**	**Z**	**p**
	9	**0**			**9**	**0**		
	F3D	xSPECT Bone	Delta		F3D	xSPECT Bone	Delta	
N	9	9	0		9	9	0	
Median	3.2	1.9	1.3		2.5	1.6	0.9	
lowest	2	1.5		**0.0039**	2	1.3		**0.0039**
highest	3.8	2.5			3.1	2.3		
95% CI Median min	2.90	1.70			2.30	1.40		
95% CI Median max	3.66	2.27			2.90	2.24		

Figure 22: *Summary of the Wilcoxon test of Q12 "Please rate your impression of diagnostic utility of the image as presented and compared to your clinical practice:" and Q13 "SPECT images only: Overall, do you accept the image and would you use it in your clinical practice?"*

Figure 23: *Bland-Altman analysis showing an overall preference of the average reader for the IQ questions.*

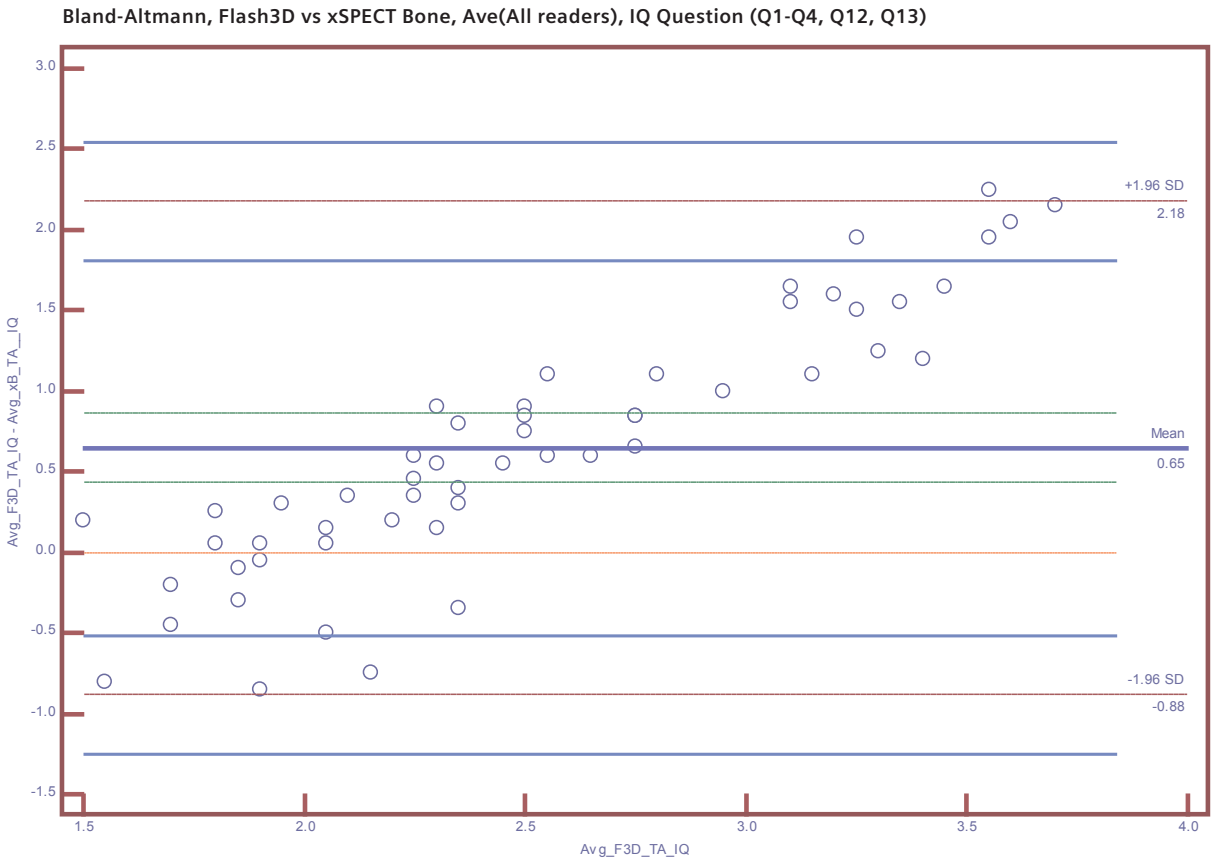

Figure 24: *Bland-Altman analysis showing an overall preference of the average reader for all questions.*

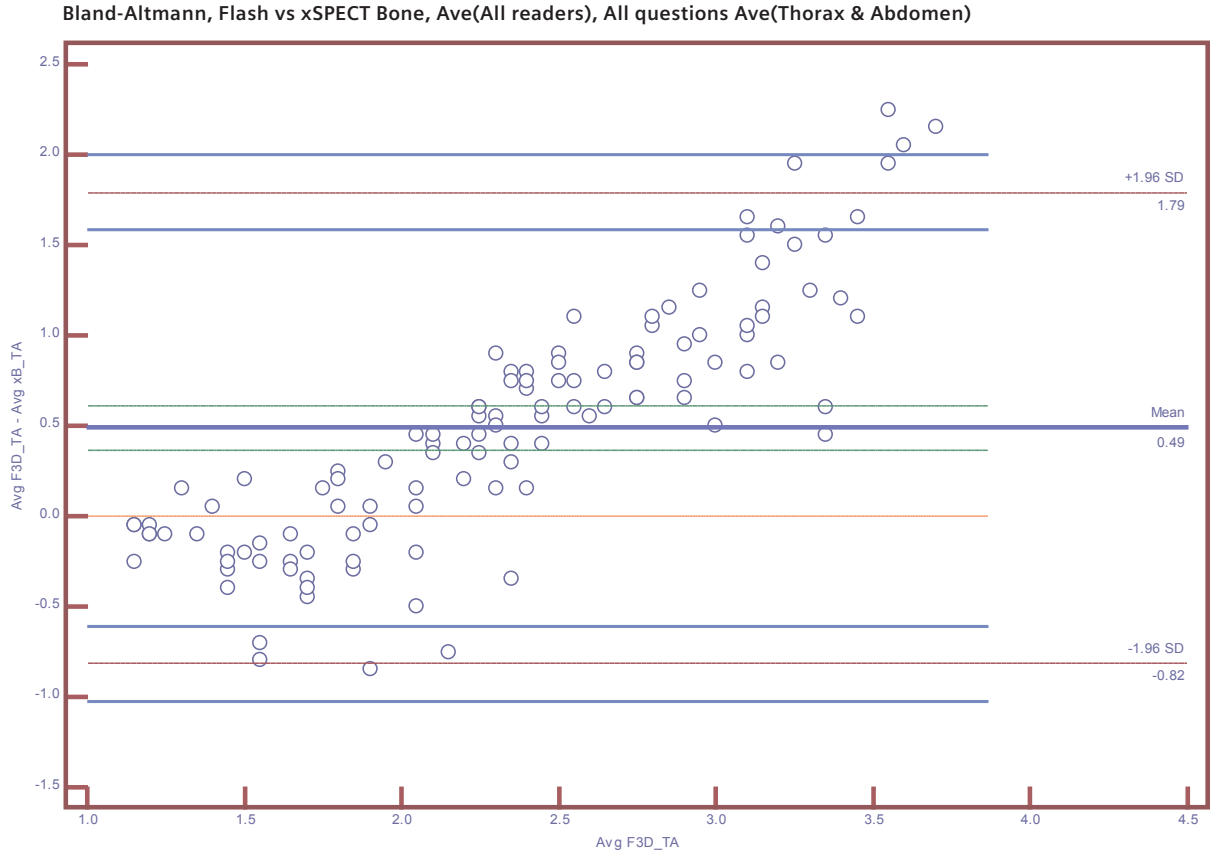

Figure 25: *Score rating from pilot evaluation of 10 readers. Rating score: 1 to 5. Smaller score is better. Questions 8-12 allowed for 6 levels, with a score of 6 denoting a decrease. The color code indicates the interpretation of the statistical results. Orange indicates a statistical non-significant difference ("NS") as the p values is larger than the expected Bonferroni corrected p value. Green indicates that xSPECT Bone ("xB") is favored while blue indicates that Flash3D ("F3D") is favored. The ICC is in red if it is significant.*

		Wilcox on signed ranks test for 2 dependent samples (ZS, JHU)							Intra Class Concordance (PH, JHU)			
Q#	Quantify differences in image quality of F3D and xSPECT Bone (xB)	Nega-tive ranks	Positive ranks	Rank ratio	Z	p	Epected p (Bonferroni corrected)	Interpre-tation	ICC Flash3 D	p- value	ICC xSPECT	p- value
1	Please rate your general impression of the noise:	47	65	0.723	-2.25	2.48E-02	3.85E-03	NS	0.1381	0.195	0.6712	0
2	Please rate your general impression of the diagnostic importance of the noise	49	54	0.907	-0.88	3.77E-01	3.85E-03	NS	0.2634	0.083	0.5805	0
3	Please rate your general impression of the image resolution?	165	1	165	-11.3	1.94E-29	3.85E-03	xB is better	0.5446	0.0004	0.2974	0.0823
4	Please rate your general impression of the diagnostic importance of the image resolution	94	19	4.947	-6.39	1.67E-10	3.85E-03	xB is better	-0.2621	0.9463	0.2459	0.0889
5	How many distinct artifact classes do you see?	13	57	0.228	-4.65	3.41E-06	3.85E-03	F3D is better	-0.0491	0.5522	0.2387	0.0544
6	Please rate your general impression of the diagnostic importance of these artifact classes:	29	46	0.630	-2.08	3.78E-02	3.85E-03	NS	-0.0213	0.5143	0.1739	0.0788
7	How many artifact classes do you see that are diagnostically disturbing or causing concern?	15	29	0.517	-1.48	1.38E-01	3.85E-03	NS	-0.0205	0.5052	-0.0803	0.6019
8	In your estimate, please rate your impression of increase in lesion detection specificity compared to Planar/Whole-body:	107	23	4.652	-6.66	2.76E-11	3.85E-03	xB is better	0.6417	0	0.1273	0.2413
9	In your estimate, please rate your impression of increase in lesion detection sensitivity compared to Planar/Whole-body:	90	30	3.000	-5.5	3.80E-08	3.85E-03	xB is better	0.6742	0	0.5275	0.0006
10	In your estimate, please rate your impression of increase in lesion conspicuity compared to Planar/Wholebody:	102	20	5.100	-7.04	1.88E-12	3.85E-03	xB is better	0.6274	0	0.5383	0.0004
11	In your estimate, please rate your impression of increase in your diagnostic confidence compared to Planar/Whole-body:	109	23	4.739	-7.47	7.97E-14	3.85E-03	xB is better	0.4072	0.0216	0.0858	0.3038
12	Please rate your impression of diagnostic utility of the image as presented & compared to your clinical practice:	117	15	7.800	-8.79	1.51E-18	3.85E-03	xB is better	0.5102	0	0.1545	0.0962
13	SPECT images only: Overall, do you accept the image and would you use it in your clinical practice?	111	27	4.111	-7.05	1.82E-12	3.85E-03	xB is better	0.4668	0.0048	0.3487	0.0012

(smaller score is better)

* ICC negative = inconclusive

Figure 25 shows the result of the analysis of both the chest and the pelvis evaluation by Dr. Z. Szabo (JHU) using a Wilcoxon signed rank test for two independent samples and the ICC values measuring concordance, analyzed by Dr. P. Huang (JHU). The results above were presented at the SNMMI 2013.[36] Please note that questions 8 through 9 specifically ask for an *impression* of the increase in lesion detection specificity and sensitivity. This is not to be equated with showing a quantifiable increase in lesion detection specificity and sensitivity. A dedicated clinical evaluation for lesion detection specificity and sensitivity may be executed at a later point in time.

The results of Aims 1 and 3 are very encouraging, but are mostly helpful to design the full evaluation by testing the length of time needed to complete the workflow, precision of questions, etc. Furthermore, that allowed us to compute the needed sample size for the full evaluation, which was completed in 2013.

Clinical example

Figure 26 shows comparison images of xSPECT Bone and Flash3D reconstruction of ^{99m}Tc MDP bone SPECT of the pelvis and lumbar vertebrae in a 66-year-old female patient with a history of adenocarcinoma of the lung. xSPECT images shows higher uptake in the metastatic lesion in the sacroiliac joint with sharp lesion margins, as well as improved visualization of pelvic bones, sacral body, ala of sacrum and spinal canal. Focal hypermetabolic metastatic lesions in L1 and L4 vertebrae are well delineated on SPECT, with higher lesion intensity in xSPECT Bone reconstruction. Small focal metastatic lesions in the acetabular margin and ischium are also better defined with higher lesion contrast with xSPECT.

Study parameters:

20 mCi ^{99m}Tc MDP inj. SPECT: 64 frames 20 sec/frame; CT: 140 kV 50 eff mAs. 3 mm slice thickness

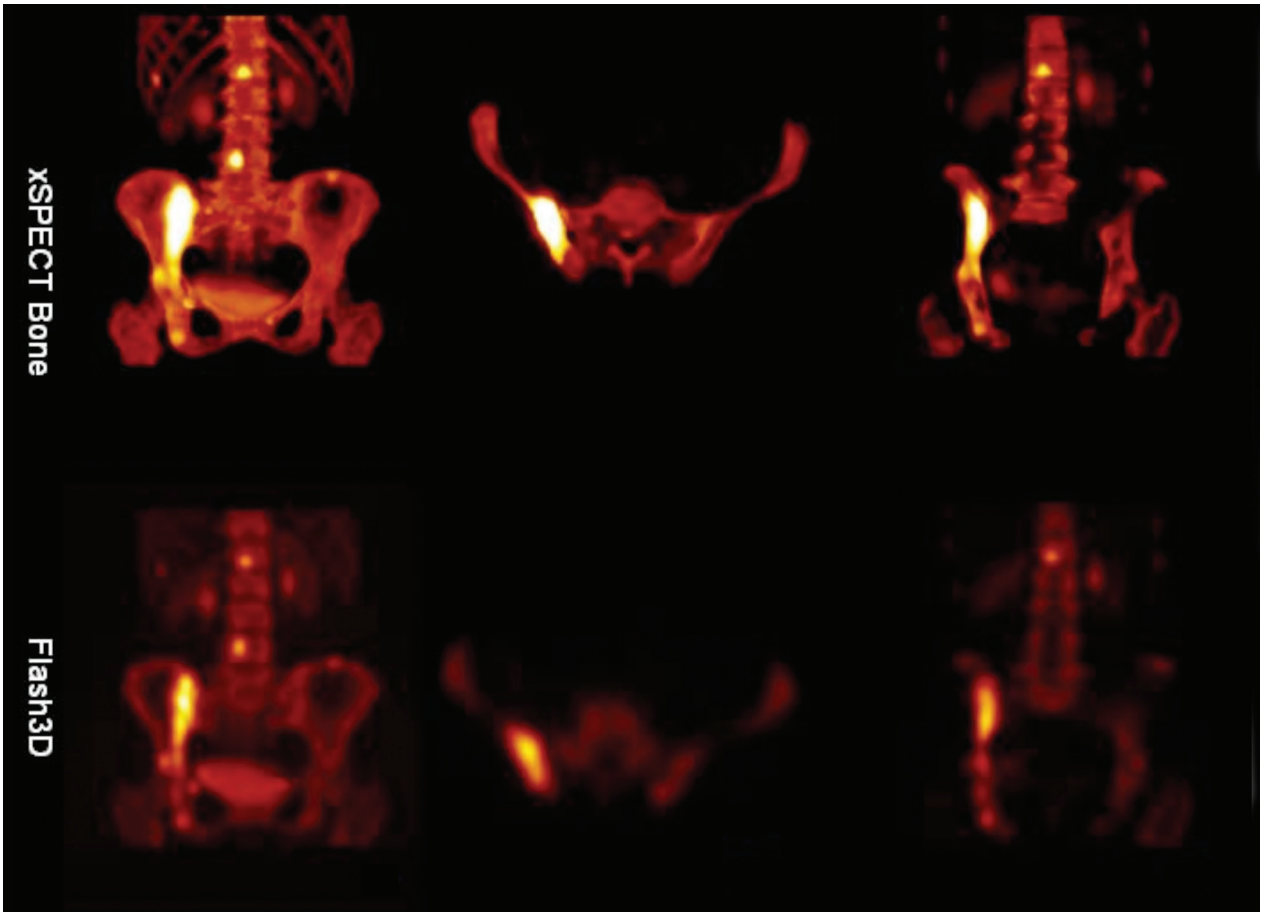

Figure 26: *Data courtesy of Johns Hopkins University, Baltimore, Maryland, USA.*

The Second Application: xSPECT Quant

xSPECT's quantitative foundation: NIST traceable calibration and rigorous data handling

In emission tomography, the data consist of photon detection events ("counts"). At the instant that an event is detected, its position on the detector, energy, and detection time are recorded. Context information from the system and patient, such as detector position, motion, and physiological trigger events are added, resulting in a list of events–listmode, or raw data. Traditionally, the data is framed into projection views containing counts-per-pixel.

Physically, the injected activity becomes distributed throughout the patient prior to the imaging time and may be regarded as a functional activity density with the preferred SI units of Bq/ml (note: 1 kBq/ml = Bq/mm^3). Correspondingly, Symbia Intevo with xSPECT technology measures the activity concentration in Bq/ml at a given reference time. The reference time chosen is the injection time.

Quantitative assessment is already important in oncology for internal dosimetry,[37,38] where it can be used for internal radiation treatment planning and monitoring. However, today only planar studies are routinely used in the clinic for this purpose, aided by a transmission and/or calibration source during acquisition. A summary of current techniques was published by Zaidi.[39] The desire for quantitative SPECT is high and extends to a plethora of isotopes. A summary of potential applications is provided by Bailey et al.[40] For instance, an upcoming need is quantitation of ^{177}Lu imaging.[41] In the case cited here, quantitation is achieved using clinically available post-processing tools. However, existing procedures are site-specific, not standardized and are cumbersome.

In general, research solutions for quantitative SPECT are possible using clinically available tools. However, such options tend to be both laborious to use as well as unique to each particular system and site.[42] Typically, they consist of some conversion of the reconstructed image from counts-per-voxel to Bq/ml. The process starts with outlining a volume-of-interest (VOI) and applying a conversion factor to the mean count within the VOI. The user must then compute and/or select a conversion factor from a list, with this selection based on the context (such as location, number of iterations, dwell time, etc.) of the VOI. This is time-consuming and potentially error prone. We seek a solution that is reliable and generalizable across systems, sites, and time, and therefore needs to be easily integrated into the clinical routine.

Any quantitative SPECT methodology has to address many problems related to accurate modeling of the imaging physics, choice of algorithm, and computer power (see, e.g., references 43-45). Additionally, other aspects must be addressed if it is to be deployed in a clinical environment, such as system stability, calibration and clinical usability, to only name a few. The xSPECT solution addresses many of these issues comprehensively, with the goal being to adapt to the tracer and selected application, and to deliver an, as accurate as possible, estimate of the 3D activity concentration *in-situ*. However, in its first release version, only ^{99m}Tc imaging using the AUTOFORM LEHR collimator is provided. Clearly, this is just the beginning, and we decided to start with the ^{99m}Tc-LEHR pair, and to first prepare infrastructure and system for future isotope-collimator pairs. A fundamental change is the adherence to the data-is-sacred principle and to apply corrections in image space during the reconstruction. This principle has significant ripple effects inside the system architecture and will be even more evident as we move on to other isotopes.

For xSPECT Quant we employ a NIST traceable calibration using a ^{57}Co source (Calibrated Sensitivity Source (CSS), Figure 27). Each CSS contains an activity accurate to within a 3% (99% CL or 2.56σ) traceable uncertainty of the known manufactured strength, which itself resides within a 15% acceptance range of the nominal 111 MBq. Following proper calibration, where the CSS is attached to the integrated source holder and extended into the FOV at a precise location (Figure 28), the xSPECT system is designed to estimate the activity concentration as an integral part of the reconstruction process. We also have an alternate method using a ^{99m}Tc protocol that doesn't offer the advantage of standardization, but can be used as fall back in case the CSS is not available. The result is an image in units of Bq/ml. No further conversion is needed. It is important to reiterate that all corrections occur in image space, allowing the data to remain unadulterated Poisson variables throughout the reconstruction process.

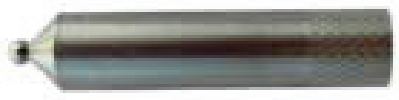

Figure 27: *Calibrated Sensitivity Source. The sphere contains the ^{57}Co source, the remainder is for safe handling of the source. The source is designed to exhibit the same scattering signature as if the spherical source was without the support body.*

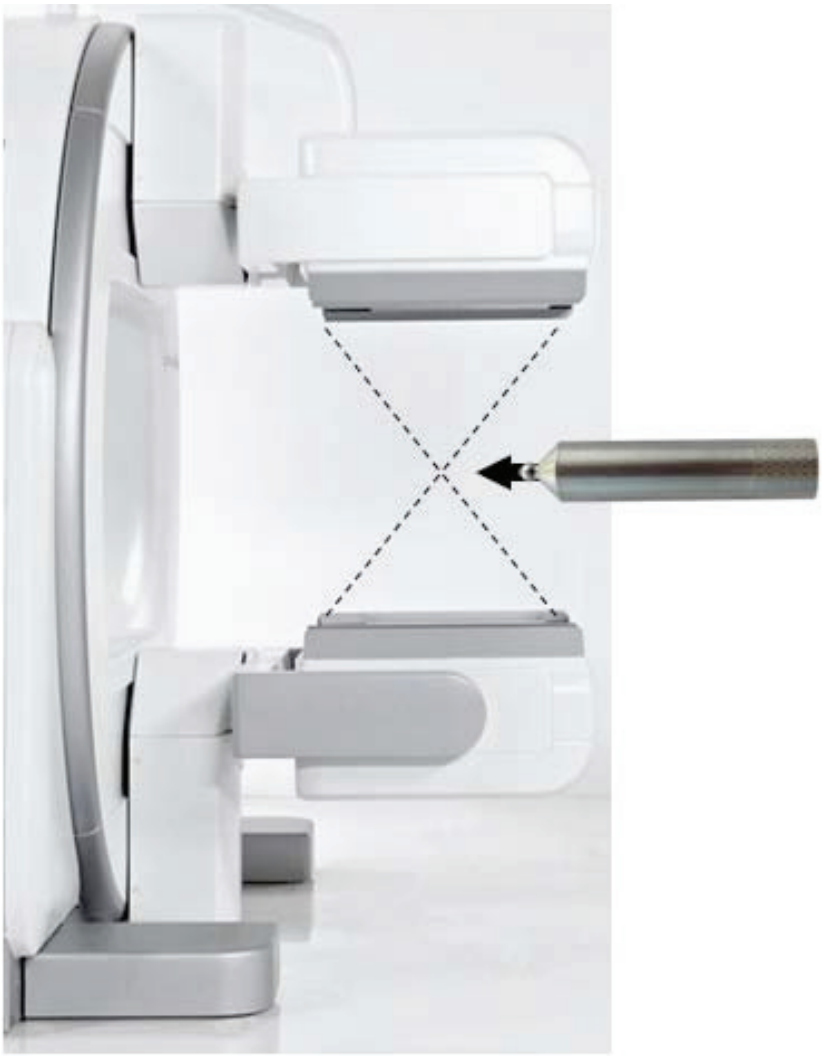

Figure 28: *CSS is inserted into Symbia Intevo and supported by the integrated source holder (not shown). The dashed lines depict the FOV.*

The CSS can also be placed in a dose calibrator in a source holder that specifies the geometry and allows for cross check between the system, the dose calibrator and the gold standard. The goal of the CSS calibration is to standardize the system sensitivity, which is essential for a quantitative results that can be compared across systems, and time.

The choice of the CG update method, the χ^2_γ objective function, as well as the improved image formation model in conjunction with the more accurate alignment of data, has advantages for quantitative accuracy and reproducibility. Furthermore, a corresponding improvement in image quality may be fostered, as these aspects complement each other.

Evaluations of xSPECT Quant

With regards to activity quantitation, preliminary results with a prototype xSPECT Bone show that the average activity concentration (AC) for Flash3D was 51.87 ± 17.38 kBq/ml (95% confidence interval (CI) 44.00–59.74 kBq/ml) corresponding to an average SUV of 6.41 ± 1.71 (95% CI 5.63–7.18 SUV). xSPECT Bone results showed an average activity of 56.70 ± 17.21 kBq/ml (95% CI 48.87–64.53 kBq/ml) and an average SUV of 7.02 ± 1.67 (95% CI 6.26–7.78 SUV). For both reconstructions, SUV correlated significantly with HU (Flash3D: r=0.536, p<0.05; xSPECT Bone: r=0.643, p<0.005). Both Flash3D and xSPECT Bone activity concentration values correlated significantly (r=0.967, p<0.0001).[45]

The results of this study show a high correlation between Flash3D and xSPECT Bone with regard to the measurement of regional activity concentration. Tracer uptake correlated with bone density which reinforces the physiological significance of this variable.

Clinical example

Figure 29 shows a possible work up of the quantitative image. The SUV method for the Bone application is not defined, and we used a similar methodology as in PET, knowing that at this point it has no demonstrated diagnostic interpretation.

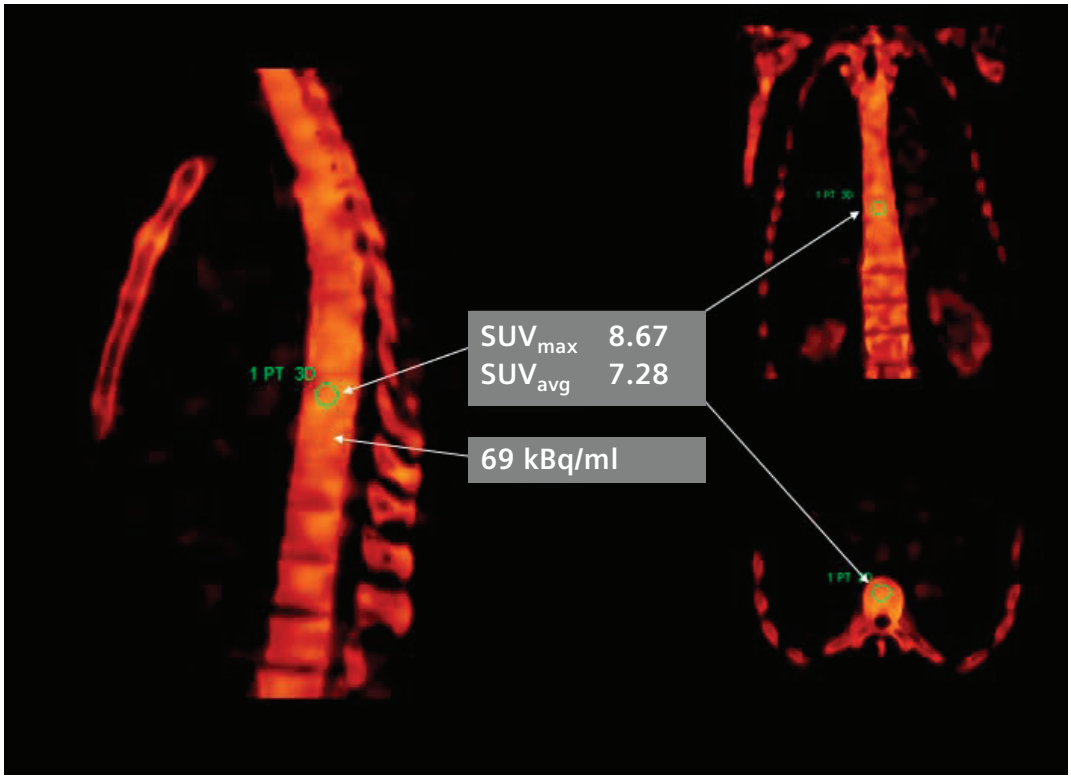

Figure 29: *xSPECT quantitative measurements in lumbar vertebrae of a patient with normal tracer distribution in thoracic and lumbar vertebrae show tracer concentration of 69 kBq/ml and average SUV of 7.28 in the center of the T9 vertebral body. Comparison with normal range shows these values to fall around the upper end of the range for normal.[48] Injected dose: 574 MBq; patient weight: 141 lb; patient height: 5'8" (Bq/ml values obtained from display in research workstation; SUV obtained from syngo TrueD).*

Data Courtesy of University of Erlangen, Erlangen, Germany.

Summary

Siemens introduced Symbia Intevo, the world's first xSPECT system, which represents a further integration between SPECT and CT by shifting the imaging viewpoint away from the SPECT Frame-of-Reference and into the CT Frame-of-Reference. The reconstruction engine was changed significantly from previous MLEM methods and is now based on the minimization of the Mighell χ^2_γ merit function using Conjugate Gradient update mechanism.

Furthermore, xSPECT employs an improved model of imaging physics and conducts all corrections in image space, allowing the data to maintain their original Poisson characteristics. To fully utilize the CT advantages, we reconstruct projections having a matrix size of 256x256, allowing for a finer spatial sampling. Despite the corresponding lower count density, this is accomplished with little noise penalty compared to the currently standard 128x128 data.

At the heart of the image projection operator is the measured PSRF, which spans the entire FOV and range of imaging distances, as well as a more accurate characterization of the detector position and improved detector performance.

Another feature of Symbia Intevo is the incorporation of the first application context-specific reconstruction for bone applications: xSPECT Bone. This improves effective image quality for relevant studies.

Furthermore, all reconstructions are quantitative *ab-initio*, a feature that is enabled when Symbia Intevo is calibrated with a NIST traceable ^{57}Co point source. This ensures system accuracy and stability, allowing for quantitative SPECT imaging for the LEHR collimator and ^{99m}Tc isotope. As a first step, the technology currently has been applied to ^{99m}Tc. However, the key advancement is that an infrastructure has been developed that now allows us to move forward with quantitative SPECT of more complex isotopes.

Image quality improvements, as well as dedicated efficiency solutions for cardiac and planar imaging, offer the ability to either lower dose or total acquisition time.

Productivity features, such as AutoQC, and ACC lower the operational burden in the clinical environment.

Acknowledgment

The author thanks James Sanders, Dr. Manojeet Bhattacharya, Dr. Amos Yahil, Dr. Jun Ma, Dr. Michal Cachovan, Dr. Xing Rong, Dr. Xinhong Ding, Dr. Ron Malmin, Dr. Partha Ghosh and Don Spence for valuable discussions, contributions and review of this document.

Glossary

Attenuation Correction (AC): Correction for patient-specific attenuation. We derive the attenuation map from CT after a patented conversion process creating the attenuation map or "mu-map", which is included in the model projection operator.

Extra Modal Information (EMI): Clinically driven information derived from a secondary modality and used in the reconstruction of the primary modality. Its primary function is to improve image quality, and assumes an accurate system model and compensation techniques that describe the image formation physics accurately.

Flash3D ("F3D"): Siemens' implementation of OSEM with 3D (transverse and axial Point Spread Response Function - PSRF). The PSRF is modeled as a Gaussian. Its width, as measured in FWHM, is a function of the collimator acceptance angle (known for each collimator) as well as the distance between emission point and detection point on the detection plane. The system provides the Radius-of-Rotation for each angle, and the remaining components that make up the total emission-detection distance are essentially computed from the known system geometry. The projection operators and thus, Flash3D, include Attenuation Correction (AC) and Scatter Correction (SC). In this context, when we refer to a NM reconstruction method we always imply that it has been corrected for attenuation, scattering, and the distance dependent 3D resolution recovery for a given collimator, unless otherwise stated.

Scatter Correction: We use energy window-based scatter correction that includes either Dual or Triple energy windows for each primary window. Since there are no relevant emissions above 140 keV for ^{99m}Tc, the isotope setting only contains a lower scatter window that is adjacent to and of the same width as the primary window.

Mu-map: The mu-map is the voxelized volume of the Linear Attenuation Coefficient (LAC) as defined in Stefan-Beer's law and measured in 1/cm. The LAC is typically referenced as the narrow beam value, measured from experiments that include essentially no scattered photons. The reconstruction uses the narrow beam value if scatter correction is selected, which is the default. Otherwise, it uses a broad beam correction factor, which is dependent on the isotope, and selected energy window width of the photopeak window. This value is automatically computed. see Attenuation Correction.

Zone-map: Indexing of each voxel in a mu-map with its tissue type, followed by a smoothing method that continuously combines the discrete threshold values for the 5 different base classes: air, adipose tissue, soft tissue, spongy bone, cortical bone. This is a method to derive context-based information. In this case, we know that DiPhosonate is injected, which binds to bone and thus it makes sense to separate bone from non-bone tissue. Different zone maps can be derived for different purposes. For instance, for phantom studies the zone map extraction can be adjusted to separate water from plastic, or a certain contrast concentration. In other cases, a zone map can be computed from other anatomical modalities.

CGAS: Base algorithm used in AR, without the zone map. Unlike Flash3D, it is not based on ML-EM, but on a Conjugate Gradient Method, and uses a chi-squared merit function modified for Poisson statistics. It also includes a 3D PSRF, but is more accurately modeled compared to the simple 3D Gaussian of Flash3D. The "A" in CGAS refers to AC and the "S" to SC. The reconstruction method estimates activity concentration, and the output unit Bq/ml, and uses a class standard sensitivity value for a given collimator.

CGZAS: Reconstruction engine is based on CGAS, but also includes context-based information using a Zone-map for zonal projections to achieve the image quality improvement, thus the "Z" in "CGZAS".

References

1 ***A. Hengerer, A. Wunder, D. J. Wagenaar, A. H. Vija, M. Shah, and J. Grimm,*** "From Genomics to Clinical Molecular Imaging," Proceedings of the IEEE, vol. 93, pp. 819- 828, 2005.

2 ***S. R. Cherry,*** "Multimodality Imaging: Beyond PET/CT and SPECT/CT," Seminars in Nuclear Medicine, vol. 39, pp. 348-353, 2009.

3 ***R. A. Brooks and G. Di Chiro,*** "Principles of computer assisted tomography (CAT) in radiographic and radioisotopic imaging," Phys Med Biol, vol. 21, pp. 689-732, Sep 1976.

4 ***S. J. Riederer, N. J. Pelc, and D. A. Chesler,*** "The noise power spectrum in computed X- ray tomography," Phys Med Biol, vol. 23, pp. 446-54, May 1978.

5 ***H. M. Hudson and R. S. Larkin,*** "Accelerated Image Reconstruction Using Ordered Subsets of Projection Data," IEEE Transactions on Medical Imaging, vol. 13, pp. 601- 609, 1994.

6 ***L. A. Shepp and Y. Vardi,*** "Maximum Likelihood Reconstruction for Emission Tomography," IEEE Transactions on Medical Imaging, vol. 1, pp. 113-122, 1982.

7 ***A. H. Vija, E. G. Hawman, and J. C. Engdahl,*** "Analysis of a SPECT OSEM reconstruction method with 3D beam modeling and optional attenuation correction: phantom studies," in IEEE Nuclear Science Symposium and Medical Imaging Conference, 2003, pp. 2662-2666.

8 ***F. Natterer,*** "On the inversion of the attenuated Radon transform," Numerische Mathematik, vol. 32, pp. 431-438, 1979.

9 ***F. Natterer,*** "Inversion of the attenuated Radon transform," Inverse Problems, vol. 17, pp. 113-119, 2001.

10 ***D. T. Wilson, B. M. W. Tsui, and J. A. Terry,*** "Non-Stationary Noise Characteristics for SPECT Images," presented at the IEEE, Nuclear Science Symposium and Medical Imaging Conference, Santa Fe, NM, USA, 1991.

11 ***J. Nuyts,*** "On estimating the variance of smoothed MLEM images," IEEE Transactions on Nuclear Science, vol. 49, pp. 714-721, 2002.

12 ***D. W. Wilson and B. M. W. Tsui,*** "Noise Properties of Filtered-Backprojection arid ML- EM Reconstructed Emission Tomographic Images," IEEE Transactions on Nuclear Science, vol. 40, pp. 1198-1203, 1993.

13 ***D. W. Wilson, B. M. W. Tsui, and H. H. Barrett,*** "Noise properties of the EM algorithm.II. Monte Carlo simulations," Physics in Medicine and Biology, vol. 39, pp. 847-871, 1994.

14 ***R. A. Fisher,*** "On an Absolute Criterion for Fitting Frequency Curves," Messenger Mathematics, vol. 41, pp. 155-160, 1912.

15 ***R. A. Fisher,*** "On the Mathematical Foundations of Theoretical Statistics," Philosophical Transactions of the Royal Society of London, vol. 222, pp. 309-368, 1922.

16 ***K. J. Mighell,*** "Parameter Estimation in Astronomy with Poisson-Distributed Data. I. The Chi-Square-Lambda Statistic," The Astrophysical Journal, vol. 518, pp. 380-393, 1999.

17 ***T. S. Press WH***, Vetterling WT & Flannery BP Numerical Recipes: Cambridge: Cambridge University Press, 2007.

18 ***B. M. W. Tsui, X. Zhao, E. C. Frey, and G. T. Gullbert,*** "Comparison Between ML-EM and WLS-CG Algorithms for SPECT IMage Reconstruction," IEEE Transactions on Nuclear Science, vol. 38, pp. 1766-1772, 1991.

19 ***H. A. Vija, Desh, Vladimir*** "Method for converting CT data to linear attenuation coefficient map data," United States Patent 6950494, 2005.

20 ***H. A. E. Vija, IL, US),*** "Acquisition window compensation for nuclear medical image reconstruction attenuation coefficient maps," United States Patent 7473900, 2009.

21 ***T. Ichihara, K. Ogawa, N. Motomura, A. Kubo, and S. Hashimoto,*** "Compton scatter compensation using the triple-energy window method for single-and dual-isotope SPECT," Journal of Nuclear Medicine, vol. 34, pp. 2216-2221, 1993.

22 ***A. H. Vija, R. Malmin, A. Yahil, J. Zeintl, M. Bhattacharya, T. D. Rempel, E. G. Hawman, and B. Bendriem,*** "A method for improving the efficiency of myocardial perfusion imaging using conventional SPECT and SPECT/CT imaging systems," in Nuclear Science Symposium Conference Record (NSS/MIC), 2010 IEEE, 2010, pp. 3433- 3437.

23 ***E. Even-Sapir,*** "Imaging of Malignant Bone Involvement by Morphologic, Scintigraphic, and Hybrid Modalities," J Nucl Med, vol. 46, pp. 1356-1367, August 1, 2005 2005.

24 ***R. A. Khan, S. Hughes, P. Lavender, M. Leon, and N. Spyrou,*** "Autoradiography of Technetium-Labelled Diphosphonate in Rat Bone," The Journal of Bone and Joint Surgery, vol. 61-B, pp. 221-224, 1979.

25 ***H. H. Barrett, J. Yao, J. P. Rolland, and K. J. Myers,*** "Model Observers for Assessment of Image Quality," Proceedings of the National Academy of Sciences of the United States of America, vol. 90, p. 7, 1993.

26 ***G. Gindi, M. Lee, A. Rangaraja, and I. G. Zubal,*** "Bayesian Reconstruction of Functional Images Using Anatomical Information as Priors," IEEE Transactions on Medical Imaging, vol. 12, pp. 670-680, 1993.

27 ***C. Comtat, P. E. Kinahan, J. A. Fessler, T. Beyer, D. W. Townsend, M. Defrise, and C. Michel,*** "Clinically Feasible Reconstruction of 3D Whole-Body PET/CT Data Using Blurred Anatomical Labels," Physics in Medicine and Biology, vol. 47, p. 20, 29 November, 2001 2002.

28 ***D. M. Higdon, J. E. Bowsher, V. E. Johnson, T. G. Turkington, D. R. Gilland, and R. J. Jaszczak,*** "Fully Bayesian estimation of Gibbs hyperparameters for emission computed tomography data," Medical Imaging, IEEE Transactions on, vol. 16, pp. 516-526, 1997.

29 ***J. E. Bowsher, V. E. Johnson, T. G. Turkington, R. J. Jaszczak, C. E. Floyd, and R. E. Coleman,*** "Bayesian reconstruction and use of anatomical a priori information for emission tomography," IEEE Transactions on Medical Imaging, vol. 15, pp. 673-686, 1996.

30 ***J. E. Bowsher, V. E. Johnson, T. G. Turkington, G. E. Floyd, Jr., R. J. Jaszczak, and R. E. Coleman,*** "Improved lesion detection and quantification in emission tomography using anatomical and physiological prior information," in Nuclear Science Symposium and Medical Imaging Conference, 1993., 1993 IEEE Conference Record., 1993, pp. 1907-1911 vol.3.

31 ***P. Calvini, P. Vitali, F. Nobili, and G. Rodriquez,*** "Enhancement of SPECT reconstructions by means of coregistered MR data," IEEE Transactions on Nuclear Science, vol. 48, pp. 750-755, 2001.

32 ***K. Strobel, C. Burger, B. Seifert, D. B. Husarik, J. D. Soyka, and T. F. Hany,*** "Characterization of Focal Bone Lesions in the Axial Skeleton: Performance of Planar Bone Scintigraphy Compared with SPECT and SPECT Fused with CT," American Journal of Radiology, vol. 188, pp. W467-W474, 2007.

33 ***E. Even-Sapir, U. Metser, E. Mishani, G. Lievshitz, H. Lerman, and I. Leibovitch,*** "The Detection of Bone Metastases in Patients with High-Risk Prostate Cancer: ^{99m}Tc-MDP Planar Bone Scintigraphy, Single- and Multi-Field-of-View SPECT, 18F-Fluoride PET, and 18F-Fluoride PET/CT," Journal of Nuclear Medicine, vol. 47, pp. 287-297, 2006.

34 ***J. Ma, A. H. Vija, M. Bhattacharya, and D. Spence,*** "A reconstruction parameter optimization scheme based on human observations," presented at the Society of Nuclear Medicine and Molecular Imaging Annual Meeting, Vancouver, Canada, 2013.

35 ***P. E. Shrout and J. L. Fleiss,*** "Intraclass Correlations: uses in Assessing Rater Reliability," Psychological Bulletin, vol. 86, p. 9, 1979.

36 ***A. H. Vija, Z. Szabo, T. Kuwert, J. Froelich, P. Bartenstein, C. Daignault, N. Gowda, O. Hadjie, H. Ilhan, and S. Yang,*** "Evaluation of image quality and clinical acceptance of HD-Bone, a novel multimodal SPECT/CT reconstruction method for Tc99m diphosphonate imaging," presented at the Society of Nuclear Medicine and Molecular Imaging Annual Meeting, Vancouver, Canada, 2013.

37 ***J. A. Siegel, S. R. Thomas, J. B. Stubbs, M. G. Stabin, M. T. Hays, K. F. Koral, J. S. Robertson, R. W. Howell, B. W. Wessels, D. R. Fisher, D. A. Weber, and A. B. Brill,*** "MIRD Pamphlet No. 16: Techniques for Quantitative Radiopharmaceutical Biodistribution Data Acquisition and Analysis for Use in Human Radiation Dose Estimates," Journal of Nuclear Medicine, vol. 40, pp. 37S-61S, 1999.

38 ***M. Stabin and A. B. Brill,*** "Physics Applications in Nuclear Medicine: 2007," Journal of Nuclear Medicine, vol. 49, pp. 20N-25, February 1, 2008 2008.

39 ***H. Zaidi, Ed.,*** Quantitative Analysis in Nuclear Medicine Imaging. New York: Springer 2006, p.^pp. Pages.

40 ***D. L. Bailey and K. P. Willowson,*** "An Evidence-Based Review of Quantitative SPECT Imaging and Potential Clinical Applications," Journal of Nuclear Medicine, vol. 54, pp. 83-89, 2013.

41 ***J.-M. Beauregard, M. S. Hofman, J. M. Pereira, P. Eu, and R. J. Hicks***, "Quantitatative 177Lu SPECT (QSPECT) imaging using a commercially available SPECT/CT system.," Cancer Imaging, vol. 11, p. 11, 2011.

42 ***J. Zeintl, A. H. Vija, A. Yahil, J. Hornegger, and T. Kuwert,*** "Quantitative Accuracy of Clinical ^{99m}Tc SPECT/CT Using Ordered-Subset Expectation Maximization with 3- Dimensional Resolution Recovery, Attenuation, and Scatter Correction," Journal of Nuclear Medicine, vol. 51, pp. 921-928, 2010.

43 ***B. M. W. Tsui, E. C. Frey, X. Zhao, D. S. Lalush, R. E. Johnston, and W. H. McCartney,*** "The importance and implementation of accurate 3D compensation methods for quantitative SPECT Phys," Physics in Medicine and Biology, vol. 39, pp. 509-530, 1994.

44 ***B. M. W. Tsui, X. Zhao, E. C. Frey, and W. H. McCartney,*** "Quantitative single-photon emission computed tomography: basics and clinical considerations, "Seminars in Nuclear Medicine, vol. 24, pp. 38-65, 1994.

45 ***R. J. Jaszczak, R. E. Coleman, and F. R. Whitehead***, "Physical factors affecting quantitative measurements using camera-based single photon emission computed tomography (SPECT)," IEEE Transactions on Nuclear Science, vol. 28, pp. 69-80, 1981.

46 ***M. Cachovan, A. H. Vija, J. Hornegger, and T. Kuwert,*** "Quantitative bone SPECT with a novel multimodal reconstruction," presented at the Society of Nuclear Medicine and Molecular Imaging Annual Meeting, Vancouver, Canada, 2013.

All comparative claims derived from competitive data at the time of printing. Data on file. Siemens reserves the right to modify the design and specifications contained herein without prior notice. As is generally true for technical specifications, the data contained herein varies within defined tolerances. Some configurations are optional. Product performance depends on the choice of system configuration.

Please contact your local Siemens Sales Representative for the most current information or contact one of the addresses listed below. Note: Original images always lose a certain amount of detail when reproduced.

Note: Original images always lose a certain amount of detail when reproduced.

*Symbia Intevo and xSPECT are not commercially available in all countries. Due to regulatory reasons their future availability cannot be guaranteed. Please contact your local Siemens organization for further details.

Siemens Healthcare Headquarters
Siemens Healthcare GmbH
Henkestraße 127
91052 Erlangen
Germany
Telephone: +49 9131 84-0
siemens.com/healthcare

MI-2706 TM.JV PDF ONLY | All rights reserved | © 11.2015 Siemens Healthcare GmbH

siemens.com/mi